Development and Validation of a new formulation of Hybrid Temporal Large Eddy Simulation

Vladimir Duffal, Benoît de Laage de Meux, Remi Manceau

▶ **To cite this version:**

Vladimir Duffal, Benoît de Laage de Meux, Remi Manceau. Development and Validation of a new formulation of Hybrid Temporal Large Eddy Simulation. Flow, Turbulence and Combustion, 2022, 108, pp.42. 10.1007/s10494-021-00264-z . hal-03206747

HAL Id: hal-03206747
https://hal.inria.fr/hal-03206747

Submitted on 23 Apr 2021

HAL is a multi-disciplinary open access archive for the deposit and dissemination of scientific research documents, whether they are published or not. The documents may come from teaching and research institutions in France or abroad, or from public or private research centers.

L'archive ouverte pluridisciplinaire **HAL**, est destinée au dépôt et à la diffusion de documents scientifiques de niveau recherche, publiés ou non, émanant des établissements d'enseignement et de recherche français ou étrangers, des laboratoires publics ou privés.

Distributed under a Creative Commons Attribution - NonCommercial - NoDerivatives| 4.0 International License

Flow, Turbulence and Combustion manuscript No.
(will be inserted by the editor)

Development and Validation of a new formulation of Hybrid Temporal Large Eddy Simulation

Vladimir Duffal · Benoît de Laage de Meux · Rémi Manceau

Received: date / Accepted: date

Abstract Hybrid RANS-LES approaches have aroused interest for years since they provide unsteady information at a reduced numerical cost compared to LES. In the hybrid context, the use of temporal filtering, to control the energy partition between resolved and modeled scales, ensures a consistent bridging between RANS and LES models. In this regard, a new formulation of Hybrid Temporal Large Eddy Simulation (HTLES) is developed, aiming at improving the theoretical foundation of the model associated with an eddy-viscosity closure. The analytical development is performed, applying the Hybrid-Equivalence criterion, and the model is calibrated in decaying isotropic turbulence. In addition, an upgraded version of the approach is proposed to improve the behavior of the model in near-wall regions, introducing a two-fold shielding function and an internal consistency constraint to provide a suitable control of the RANS-to-LES transition. Applying HTLES to the k–ω SST model, the validation process is carried out on channel and periodic-hill flows, over a range of grids and Reynolds numbers. The predictive accuracy and the robustness to grid coarsening are assessed in these cases, ensuring that HTLES offers a cost-saving alternative to LES.

Keywords Turbulence modeling · Hybrid RANS-LES · Temporal filtering · HTLES · Shielding functions · Channel and periodic-hill flows

1 Introduction

In a wide range of industrial applications, the capability of computational fluid dynamics to accurately represent turbulent flows and provide unsteady information is a key issue. For instance, in the nuclear industry, the prediction of unsteady hydraulic loads is a major concern to conduct safety analysis in pressurized water reactors. Nowadays, common approaches for modeling turbulence are Reynolds-Averaged Navier-Stokes (RANS), Large-Eddy Simulation (LES) and hybrid RANS-LES. On the one hand, RANS models are currently used to design and conduct industrial studies due to their wide applicability and low-computational cost, but they do not provide the quantities of interest for unsteady analysis. On the other hand, LES provides the adequate level of description, explicitly resolving the most energetic part of the turbulent spectrum. However, the computational cost is prohibitive at industrial scales, notably in the vicinity of the wall where the grid size requirements of LES remain out of reach in most configurations, despite the ever-increasing power of computers (see, e.g., the estimate of Spalart [46]).

In this context, hybrid RANS-LES approaches offer the best potential to reach the compromise between the reduced numerical cost of RANS and the capability of LES to provide unsteady information. LES captures large-scale structures in regions of interest, while regions where LES is not required or too CPU-demanding are treated in RANS mode. The present paper focuses on continuous hybrid RANS-LES approaches based on one set of equations, since these methods are suitable and easily used from an engineering point of view. For the past two decades, many hybrid approaches have been developed, such as Detached-Eddy Simulation (DES) [45], Partially Integrated Transport Model (PITM) [10],

Vladimir Duffal (corresponding author)
E-mail: vladimir.duffal@edf.fr

Vladimir Duffal · Benoît de Laage de Meux
EDF R&D, MFEE Dept., 6 quai Watier, 78400 Chatou, France
E-mail: benoit.de-laage-de-meux@edf.fr

Vladimir Duffal · Rémi Manceau
CNRS, Université de Pau et des Pays de l'Adour, E2S UPPA, INRIA, équipe CAGIRE, LMAP, Pau, France
E-mail: remi.manceau@univ-pau.fr

Partially Averaged Navier-Stokes (PANS) [19], or Scale-Adaptative Simulation (SAS) [32], among the most emblematic models (for more details, refer to the recent review of Chaouat [9]).

Within this background, the definition of a rigorous formalism for continuous hybrid RANS-LES approaches is highly desirable to favour the modeling of the subfilter stresses, to determine the relations between the subfilter variables and the statistically averaged variables of the underlying RANS closure, and to understand the phenomenology of the resolved motion. In this context, the favorable framework to analytically develop hybrid approaches is to use a consistent filtering formalism, providing a continuous transition from a filtered (LES) to a statistical (RANS) description. To ensure the consistency of the filtering operator with the statistical averaging in a wide range of configurations, Fadai-Ghotbi *et al.* [15] and Manceau [30] showed that the use of temporal filtering in lieu of spatial filtering is particularly suitable for defining the LES operator. In order to avoid confusion, it is worth mentioning from the outset that the use of the denomination *temporal* in the name of the approach (HTLES, Hybrid Temporal LES) only refers to the fact that the analytical developments are based on a temporal filtering formalism, which allows the temporal LES equations to tend to the RANS equations in inhomogeneous flows. In practice, the model does not imply any explicit filtering, but simply involves terms that vary as a function of the ratio between the time scale of turbulence, k/ε, and the cutoff frequency related to the numerical scheme, which depends on both the time step dt and the grid step Δ, as presented below.

Fadai-Ghotbi *et al.* [15] proposed a temporal version of PITM (TPITM), by substituting temporal filtering for spatial filtering, and obtained transport equations of the same form as those of the original PITM [10], thus confirming the generality of this approach. However, applications of the method [15] showed that it can, in some cases that do not feature detached shear layers, such as turbulent channel flows, have difficulty in converging to a permanent state and can even tend towards a pseudo-laminar solution. This issue was first addressed by Fadai-Ghotbi *et al.* [14] using a dynamic procedure. Attributing this problem to the indirect control of the energy partition through the dissipation equation, an alternative solution has been proposed by Friess *et al.* [16], who transferred the hybridization term into the turbulent energy equation, introducing a Hybrid-equivalence (H-equivalence) criterion between hybrid approaches. Thereafter, Manceau [30] developed the Hybrid Temporal Large Eddy Simulation (HTLES), a continuous hybrid approach derived from TPITM, where the hybridization term in the energy equation is based on a time scale driven by the modeled-to-total energy ratio. This formulation of HTLES has already been validated in flows around a rectangular cylinder by Tran *et al.* [49] and around a valve with a fixed lift by Afailal *et al.* [2], showing promising results. However, the resolution of the near-wall region of the flow was not extensively validated in these previous studies. In contrast, in the present paper, great attention is paid to the explicit resolution of the whole boundary layer, as discussed below.

In addition, recent developments and validation of HTLES are presented, in order to strengthen and improve the model for the purpose of industrial applications, i.e. capable of dealing with wall-bounded flows at high Reynolds numbers, and offering a cost-saving alternative to LES. Applying the H-equivalence criterion [16], a new formulation of HTLES with an eddy-viscosity model as the closure is proposed, refining its theoretical foundations. Although a large part of the literature on which the present work is based has been conducted with Reynolds-stress models [10, 14–16], the choice has been made here to use an eddy-viscosity model common in the industry, the k–ω SST model [33]. Indeed, our objective is to develop a hybrid RANS-LES model that is simple and robust enough to be attractive for the current activities of engineers. The extension of the approach to other models is left for future work. For the sake of simplicity, a standard k–ε closure is used to present the theoretical analysis, which is then extended to the k–ω SST model. The LES branch of HTLES is based on the same closure as the RANS branch, sensitizing the model to the filter width via the hybridization function. Then, a new shielding function and an internal consistency constraint are introduced to improve the behavior of the model in near-wall regions. Channel flows at moderate and high Reynolds numbers are investigated to evaluate the upgraded formulation of HTLES in boundary-layer-like flows. The model is finally validated in periodic-hill flows, a standard benchmark test case, which has already been studied with many hybrid approaches [23], including the PITM model [8, 12].

The paper is organized as follows: after introducing the modeling framework based on temporal filtering in section 2, the third section is devoted to the development of the new formulation of HTLES. In section 4, the upgraded formulation is proposed to improve the behavior of the model for wall-bounded flows. Finally, the k–ω SST HTLES model is validated in section 5, on channel and periodic-hill flows, with sensitivity study to the grid and the Reynolds number.

2 Modeling framework

2.1 Temporal filtering

In filtered approaches, the instantaneous velocity is decomposed into a resolved part and a residual part, $U_i^* = \widetilde{U}_i + u_i''$. The resolved part is obtained by the application of a filtering operator $\widetilde{\cdot}$, such that

$$\widetilde{U}_i(\mathbf{x},t) = \int_{\mathscr{D}} \int_{-\infty}^{t} \mathscr{G}(\mathbf{x},\mathbf{x}',t,t') U_i^*(\mathbf{x}',t') d\mathbf{x}' dt', \tag{1}$$

where $\mathscr{G}$ is the filter kernel in a spatial domain $\mathscr{D}$ and the time interval $[-\infty;t]$ (causal filter). This definition encompasses spatial filtering, with a filter kernel $\mathscr{G}(\mathbf{x},\mathbf{x}',t,t') = \mathscr{G}_\Delta(\mathbf{x},\mathbf{x}')\ \delta(t'-t)$, where δ is the Dirac delta function; and temporal filtering, for which the filter kernel is of the form $\mathscr{G}(\mathbf{x},\mathbf{x}',t,t') = \mathscr{G}_{\Delta_T}(\mathbf{t},\mathbf{t}')\ \delta(\mathbf{x}'-\mathbf{x})$.

In order to favour the modeling of the subgrid stresses and analytically develop hybrid RANS-LES formulations, a consistent filtering formalism is used to provide a continuous transition from a RANS statistical description to a LES filtered description. The consistency of the filtering operator means that when the filter width goes to zero, the instantaneous quantities are recovered (DNS limit), and when the filter width goes to infinity, the filtered quantities go to the statistically-averaged quantities (RANS limit). It is worth noting that the choice of the filtering operator depends on the situation:

(i) In the case of spatial filtering, filtered quantities tend to spatially-averaged quantities when the filter width goes to infinity. Therefore, the consistency is ensured for homogeneous flows only, since statistical and spatial averaging are equivalent in such a case, but this condition is not fulfilled in industrial applications.

(ii) In contrast, following Fadai-Ghotbi *et al.* [15], temporal filtering provides a consistent formalism for the wide class of statistically stationary inhomogeneous flows, which corresponds to many industrial configurations. When the temporal filter width goes to infinity, the time-filtered quantities go to the long-time averaged quantities equivalent to statistically-averaged quantities as a result of the ergodicity hypothesis for stationary flows. Moreover, for non-stationary flows, the consistency between unsteady RANS (URANS) and temporal LES (TLES) was shown by Manceau [30].

It is important to note that, in practice, since there is no explicit filter applied during the simulation, approaches based on temporal filtering, whether temporal LES (TLES) or hybrid temporal LES (HTLES), do not fundamentally differ from spatial approaches. The interest of the temporal framework lies, as indicated above, in the extension of the validity of the hybridization between LES and RANS to inhomogeneous flows, and makes it possible to derive relationships between the model parameters and the cutoff frequency in an analytical way.

In order to preserve Galilean invariance, Fadai-Ghotbi *et al.* [15] defined the *uniform temporal filter*, $\mathscr{G}(\mathbf{x},\mathbf{x}',t,t') = \delta(\mathbf{x}-\mathbf{x}'+(t'-t)\mathbf{V}_{\text{ref}})\mathscr{G}_{\Delta_T}(t,t')$, where $\mathscr{G}_{\Delta_T}$ is the temporal filter kernel, and $\mathbf{V}_{\text{ref}}$ is a reference velocity. $\mathbf{V}_{\text{ref}} = 0$ must be chosen in the reference frame in which the assumption of statistical stationarity is verified. Hence, the consistency of the filtering operator $\widetilde{\cdot}$ with the statistical averaging operator $\overline{\cdot}$ can be demonstrated [15] within the limit of an infinite filter width Δ_T, such that

$$U_i(\mathbf{x}) = \lim_{\Delta_T\to+\infty} \widetilde{U}_i(\mathbf{x},t) = \lim_{\Delta_T\to+\infty} \int_{-\infty}^{t} \mathscr{G}_{\Delta_T}(t,t')U_i^*(\mathbf{x},t')dt', \tag{2}$$

where $U_i = \overline{U_i^*}$ denotes the statistical average of the instantaneous velocity. The total and resolved fluctuations are defined by u_i and u_i', respectively. It yields

$$U_i^* = U_i + u_i = \widetilde{U}_i + u_i'' \quad \text{and} \quad u_i = u_i' + u_i''. \tag{3}$$

Since the temporal filter satisfies linearity and preservation of the constants, and assuming commutativity with differential operators as in spatial LES, the general filtering approach of Germano [17] can be applied to define the equation for the filtered velocity $\widetilde{U}_i$ and the transport equations for the subfilter stress (sfs) tensor $\tau_{ij\text{sfs}} = \widetilde{u_i''u_j''}$. In order to simplify the derivations, it is assumed herein that the temporal filter is a spectral cutoff filter, but Fadai-Ghotbi *et al.* [15] demonstrated that, for any type of filter, using generalized central moments, these equations are of the same form as the RANS equations (i.e., the equations for the statistically-averaged velocity U_i and the total Reynolds stress $R_{ij} = \overline{u_iu_j}$). Similarly, the transport equation for the subfilter energy $k_{\text{sfs}} = \frac{1}{2}\tau_{ii\text{sfs}}$ is formally identical to the equation for the total turbulent energy $k = \frac{1}{2}R_{ii}$.

This formal similarity, associated with the consistency of the filtering operator, suggests that a sensitization of the model to the filter width can provide a solid foundation for bridging RANS and LES models. These properties are fundamental to ensure the continuous transition between RANS and LES modes, and notably to make sure that the hybrid model tends to the exact RANS closure in RANS mode, as shown below in section 3.5.

In this filtering framework, the total energy k is exactly decomposed into a resolved energy k_{r} and a modeled energy k_{m}, such that

$$k = k_{\text{r}} + k_{\text{m}}, \qquad \text{where} \quad k = \frac{1}{2}\overline{u_iu_i},\ \ k_{\text{r}} = \frac{1}{2}\left(\overline{\widetilde{U}_i\,\widetilde{U}_i} - \overline{\widetilde{U}_i}\,\overline{\widetilde{U}_i}\right) = \frac{1}{2}\overline{u_i'u_i'},\ \ k_{\text{m}} = \overline{k_{\text{sfs}}} = \frac{1}{2}\overline{\widetilde{u_i''u_i''}}. \tag{4}$$

As mentioned above, to simplify the analysis, $\mathscr{G}_{\Delta_T}$ is considered herein as a cutoff filter, and its cutoff frequency ω_c divides the Eulerian energy spectrum $E_T(\omega)$ into filtered and residual scales, as illustrated in Fig. 1. The energy partition in the frequency domain is defined as

$$k = \int_0^\infty E_T(\omega)d\omega, \quad k_{\text{r}} = \int_0^{\omega_c} E_T(\omega)d\omega, \quad k_{\text{m}} = \int_{\omega_c}^\infty E_T(\omega)d\omega. \tag{5}$$

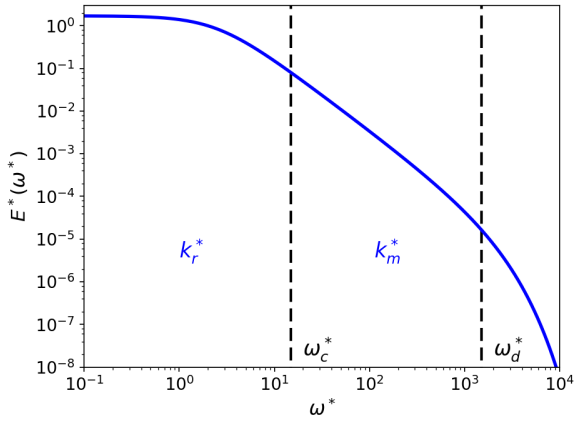

Fig. 1 Sketch of the partition of the Eulerian energy spectrum in a filtered approach. Quantities are made nondimensional using the turbulent kinetic energy k and the dissipation rate ε.

In standard LES, the modeled energy is generally neglected, since the cutoff frequency is located well inside the inertial region (the modeled-to-total energy ratio $r = k_{\mathrm{m}}/k < 0.2$ according to the Pope's definition [36] of LES). In contrast, in hybrid approaches, since the location of the cutoff frequency may vary in the turbulent spectrum, from ω_c in the inertial range down to $\omega_c = 0$ at the RANS limit ($r = 1$), it is necessary to provide an accurate modeling of the subfilter scales.

2.2 Modeling of the subfilter scales using an eddy-viscosity closure

Using the general filtering approach of Germano [17], the equations for the filtered velocity are as follows

$$\frac{\partial \widetilde{U}_i}{\partial x_i} = 0 \quad \text{and} \quad \frac{D\widetilde{U}_i}{Dt} = -\frac{1}{\rho}\frac{\partial \widetilde{P}}{\partial x_i} + \nu \frac{\partial^2 \widetilde{U}_i}{\partial x_j \partial x_j} - \frac{\partial \tau_{ij\mathrm{sfs}}}{\partial x_j}, \tag{6}$$

where $\widetilde{P}$ is the filtered pressure and ν is the kinematic viscosity. When the filter width is variable in space or time, the error due to the non-commutativity of the filter and the differential operators is considered negligible, as usual in LES [40].

In the present work, an eddy-viscosity model is used to solve the closure problem, for its numerical robustness and reduced computational cost compared to more complex modeling approaches. The Boussinesq assumption postulates that the subfilter stress tensor is proportional to the resolved strain rate tensor $\widetilde{S}_{ij}$, introducing the subfilter viscosity ν_{sfs}, such that

$$\tau_{ij\mathrm{sfs}} = -2\nu_{\mathrm{sfs}}\widetilde{S}_{ij} + \frac{2}{3}k_{\mathrm{sfs}}\delta_{ij}. \tag{7}$$

The exact transport equation for k_{sfs} can be obtained by contracting the transport equation for $\tau_{ij\mathrm{sfs}}$ [15], leading to

$$\frac{Dk_{\mathrm{sfs}}}{Dt} = P_{\mathrm{sfs}} + D_{k\mathrm{sfs}} - \varepsilon_{\mathrm{sfs}}, \tag{8}$$

where P_{sfs} denotes the production of k_{sfs}, $D_{k\mathrm{sfs}}$ the diffusion term and $\varepsilon_{\mathrm{sfs}}$ the subfilter dissipation rate. Since all these terms can not be explicitly resolved, a turbulence model is developed in the following section, in the context of two-equation closures. Notably, the second transported variable, which determines the turbulent scales, deserves a particular attention.

3 A new formulation of HTLES with eddy-viscosity closure

3.1 Temporal PITM and H-equivalence

To model the unresolved scales, Fadai-Ghotbi *et al.* [15] proposed a temporal version of the Partially Integrated Transport Model (PITM), originally developed by Chaouat and Schiestel [10] in the framework of spatial filtering. The development of TPITM is based on a theoretical analysis, considering a partition of the frequency domain into three regions as shown in Fig. 1: resolved $[0, \omega_c]$, modeled $[\omega_c, \omega_d]$ and dissipative $[\omega_d, \infty]$ scales. ω_c is the cutoff frequency

of the temporal filter and ω_d is defined as a frequency sufficiently large for the amount of energy in the dissipative region to be negligible compared to the energy in the modeled region. Hence, by integrating the equation of the Eulerian temporal energy spectrum in the range $[\omega_c, \omega_d]$, it can be shown [15] that the modeled turbulent viscosity ν_m, energy k_m and dissipation rate ε_m satisfy the following equations

$$\nu_\mathrm{m} = C_\mu \frac{k_\mathrm{m}^2}{\varepsilon_\mathrm{m}}, \tag{9}$$

$$\begin{cases} \dfrac{Dk_\mathrm{m}}{Dt} = P_\mathrm{m} + D_{k\mathrm{m}} - \varepsilon_\mathrm{m}, \\ \dfrac{D\varepsilon_\mathrm{m}}{Dt} = C_{\varepsilon 1}\dfrac{\varepsilon_\mathrm{m}}{k_\mathrm{m}} P_\mathrm{m} + D_{\varepsilon\mathrm{m}} - C_{\varepsilon 2}^P(r)\dfrac{\varepsilon_\mathrm{m}^2}{k_\mathrm{m}}, \end{cases} \tag{10}$$

where P_m denotes the production of k_m, and $D_{k\mathrm{m}}$ and $D_{\varepsilon\mathrm{m}}$ stand for the diffusion of k_m and ε_m, respectively. These equations take the same form as those of the original PITM derived in the wavenumber space [10,41]. The RANS-LES transition is controlled by the hybridization function

$$C_{\varepsilon 2}^P(r) = C_{\varepsilon 1} + r(C_{\varepsilon 2} - C_{\varepsilon 1}), \tag{11}$$

driven by the ratio of modeled-to-total energy $r = k_\mathrm{m}/k$. It is worth pointing out that, when the energy ratio r goes to 1, $C_{\varepsilon 2}^P(1) = C_{\varepsilon 2}$ and the hybrid formulation tends to a k–ε RANS model [25], with the coefficients C_μ, $C_{\varepsilon 1}$ and $C_{\varepsilon 2}$ (provided that the consistency of the filtering operator is ensured). When $r < 1$, the modeled energy and viscosity are reduced, and the model gradually switches to the LES mode. However, since the level of modeled energy is not directly controlled through the energy equation but only indirectly through the hybridization function in the dissipation equation, the resolved turbulence is not always sustained by TPITM [15]. In the absence of an additional correction such as the dynamic procedure [14], it can lead to a pseudo-laminarization of the computed flows, notably for flows which are not dominated by the Kelvin-Helmholtz instability.

To address this issue, Friess *et al.* [16] transferred the hybridization function into the destruction term of the energy equation, which is favorable in term of robustness, while preserving a H-equivalence criterion (H stands for hybrid) between the approaches. This criterion ensures that two hybrid approaches lead to the same partition of energy for the same filter width, and tend to the same RANS model when the filter width goes to infinity. In this context, the development of the Equivalent-DES method by Friess *et al.* [16] and the Hybrid Temporal LES (HTLES) by Manceau [30] meets the specifications: these models are H-equivalent to the TPITM model, using the same closure but involving a hybridization function $\psi(r)$ in the destruction term of the k_m-equation rather than a variable coefficient $C_{\varepsilon 2}^P(r)$ in the ε_m-equation. To ensure H-equivalence, they showed within a perturbation analysis that infinitesimal variations of the hybridization functions $C_{\varepsilon 2}^P(r)$ and $\psi(r)$ lead to the same infinitesimal variation of the modeled energy k_m.

It is important to note that, in the TPITM system (Eq. 10), the variable ε_m transported by the second equation is the dissipation rate of the modeled energy k_m, since it is the destruction term involved in the k_m-equation. In the HTLES system, the introduction of $\psi(r)$ in this destruction term implies that the second variable is not the dissipation rate anymore. Therefore, for the sake of clarity, a new notation ε_m^* is introduced for the second transported variable, such that the general form of the model developed by Friess *et al.* [16] is written here as

$$\begin{cases} \dfrac{Dk_\mathrm{m}}{Dt} = P_\mathrm{m} + D_{k\mathrm{m}} - \psi(r)\varepsilon_\mathrm{m}^*, \\ \dfrac{D\varepsilon_\mathrm{m}^*}{Dt} = C_{\varepsilon 1}\dfrac{\varepsilon_\mathrm{m}^*}{k_\mathrm{m}} P_\mathrm{m} + D_{\varepsilon\mathrm{m}}^* - C_{\varepsilon 2}\dfrac{{\varepsilon_\mathrm{m}^*}^2}{k_\mathrm{m}}, \end{cases} \tag{12}$$

where $D_{\varepsilon\mathrm{m}}^*$ stands for the diffusion of ε_m^*, and $\psi(r)\varepsilon_\mathrm{m}^* = \varepsilon_\mathrm{m}$ is the dissipation rate of k_m.

3.2 Evaluation of the modeled viscosity

For the TPITM (Eq. 10) and HTLES (Eq. 12) systems, the definition of the modeled viscosity ν_m deserves attention. Following the original development of the PITM approach [10,41], the modeled viscosity can be estimated in wavenumber space according to Heisenberg's hypothesis [22], leading to

$$\nu_\mathrm{m} = C_\nu \int_{\kappa_c}^{\infty} \kappa^{-3/2} E(\kappa)^{1/2} d\kappa, \tag{13}$$

where $E(\kappa)$ is the spatial energy spectrum, κ_c is the cutoff wavenumber, and C_ν is a coefficient. We propose here to reformulate this expression in the frequency domain, recalling that the spatial energy spectrum and the Eulerian

temporal energy spectrum are related by $dk = E(\kappa)d\kappa = E_T(\omega)d\omega$. By analysing the Eulerian frequency spectrum, Tennekes [48] proposed the dispersion relation $\omega = U_s\kappa$, where U_s is the sweeping velocity. In the presence of a mean flow, the sweeping velocity is defined as $U_s = U + \gamma\sqrt{k}$, where U is the mean velocity magnitude and $\gamma\sqrt{k}$ denotes the characteristic velocity of the energetic eddies, with γ a coefficient. The introduction of the previous relations in Eq. (13) leads to

$$\nu_{\mathrm{m}} = C_\nu \int_{\omega_c}^{\infty} U_s \omega^{-3/2} E_T(\omega)^{1/2} d\omega. \tag{14}$$

To simplify this expression, some assumptions are made, based on the theoretical framework used by Schiestel and Dejoan [41] to develop the PITM model: the cutoff wavenumber κ_c is in the inertial range of a Kolmogorov spectrum $E(\kappa) = C_K \varepsilon^{2/3} \kappa^{-5/3}$, where ε is the total dissipation rate and C_K is the Kolmogorov coefficient. Using the assumption of an equilibrium Eulerian spectrum [48], and the dispersion relation $\omega = U_s\kappa$, the temporal energy spectrum is defined as $E_T(\omega) = C_K \varepsilon^{2/3} {U_s}^{2/3} \omega^{-5/3}$, and the cutoff frequency ω_c is in inertial range of the spectrum. Therefore, the modeled energy given by Eq. (5) can be estimated as

$$k_{\mathrm{m}} = \int_{\omega_c}^{\infty} E_T(\omega) d\omega = \frac{3C_K}{2} \varepsilon^{2/3} U_s^{2/3} \omega_c^{-2/3}. \tag{15}$$

Using this expression, we show that the modeled viscosity given by Eq. (14) in the frequency space can be evaluated as

$$\nu_{\mathrm{m}} = \frac{3}{4} C_\nu C_K^{1/2} \varepsilon^{1/3} U_s^{4/3} \omega_c^{-4/3} = \frac{1}{3} C_\nu C_K^{-3/2} \frac{k_{\mathrm{m}}^2}{\varepsilon} = C_\mu \frac{k_{\mathrm{m}}^2}{\varepsilon}, \tag{16}$$

with $C_\mu \simeq 1/3 C_\nu C_K^{-3/2}$. Note that this relation is exactly the same as the one obtained in the wavenumber space in the framework of PITM [41].

In the TPITM approach, the physical dissipation rate ε is evaluated as the modeled dissipation rate ε_{m}, solution of the second transport equation. Actually, it is assumed that the cutoff frequency is in the inertial range of an Eulerian temporal energy spectrum, which means that the resolved dissipation is negligible, such that $\varepsilon_{\mathrm{m}} = \varepsilon$. Hence, the definition of the modeled viscosity given by Eq. (9) in the TPITM formulation is equivalent to Eq. (16), which is consistent with the original PITM formulation [41].

The situation is different for HTLES. In the original development of the system of equations (12), Friess *et al.* [16] assumed that the second transported variable $\varepsilon_{\mathrm{m}}^*$ remains equal to ε to conduct their theoretical analysis. We propose here to dispense with this assumption, since the dissipation term of the k_{m}-equation is

$$\varepsilon_{\mathrm{m}} = \psi(r)\varepsilon_{\mathrm{m}}^*, \tag{17}$$

such that, in LES mode, for which the resolved part of dissipation is negligible, the correct relation is $\psi(r)\varepsilon_{\mathrm{m}}^* = \varepsilon$. Therefore, the expression $\nu_{\mathrm{m}} = C_\mu k_{\mathrm{m}}^2/\varepsilon_{\mathrm{m}}^*$ used in previous versions of HTLES is replaced here by

$$\nu_{\mathrm{m}} = C_\mu \frac{k_{\mathrm{m}}^2}{\psi(r)\varepsilon_{\mathrm{m}}^*}. \tag{18}$$

Hence, the destruction term of the k_{m}-equation (Eq. 12) and the dissipation term in the definition of modeled viscosity (Eq. 18) are exactly the same, corresponding to the modeled dissipation rate, in the same way as for the TPITM formulation.

3.3 Consistent application of H-equivalence to the eddy-viscosity closure

To ensure H-equivalence [16] between HTLES and TPITM, the objective is to identify a relation between the hybridization functions $C_{\varepsilon 2}^P(r)$ and $\psi(r)$, which appear in (10) and (12), respectively, in order to provide the same level of modeled energy k_{m} for the two approaches. The interest of H-equivalence can be easily understood in the framework of eddy-viscosity models by looking at Eq. (16): the level of eddy-viscosity injected in the momentum equation is uniquely a function of k_m, such that two approaches giving the same field of k_m will give very similar velocity fields.

In this regard, infinitesimal perturbations $\delta C_{\varepsilon 2}^P$ and $\delta\psi$ are introduced into the TPITM system of equations (9, 10) and the HTLES system (12, 18), respectively, and the resulting infinitesimal variations δk_{m} of the modeled energy are analysed. In this way, a relation between $\delta C_{\varepsilon 2}^P$ and $\delta\psi$ can be identified to make sure that the perturbation δk_{m} of the modeled energy is the same for the two systems of equations. Integrating this relation between the RANS state ($C_{\varepsilon 2}^P(1) = C_{\varepsilon 2}$; $\psi(1) = 1$ and $k_m = k$) and some arbitrary LES state, the expression for $\psi(r)$ is obtained for HTLES to be H-Equivalent to TPITM.

This perturbation analysis is intractable in general configurations, but can be analytically solved using some simplifying hypotheses, as shown by Friess *et al.* [16]: homogeneous turbulence; inhomogeneous turbulence in a straight

duct flows, assuming that ε_m is not affected by the variations of the coefficients; inhomogeneous turbulence in a straight duct flows without this assumption but for eddy-viscosity models only. For this three different cases, Friess *et al.* [16] obtained three slightly different expressions for $\psi(r)$ as a function of the energy ratio r:

$$\psi(r) = 1 + (C_{\varepsilon 2} - C_{\varepsilon 1})(1-r), \quad \psi(r) = 1 + \left(\frac{C_{\varepsilon 2}}{C_{\varepsilon 1}} - 1\right)(1-r), \quad \psi(r) = 1 + \left(\frac{C_{\varepsilon 2}}{C_{\varepsilon 1}} - 1\right)\left(1 - r^{C_{\varepsilon 1}/C_{\varepsilon 2}}\right). \tag{19}$$

In contrast, based on the present formulation of the HTLES model, for which the main modifications lie in the definition of the second transported variable (Eq. 17) and the presence of the $\psi(r)$ function in the definition of the modeled viscosity (Eq. 18), the perturbation analysis is carried out again and leads to a unique expression in the three cases,

$$\psi(r) = \frac{C_{\varepsilon 2}}{C^P_{\varepsilon 2}(r)} = \frac{C_{\varepsilon 2}}{C_{\varepsilon 1} + r(C_{\varepsilon 2} - C_{\varepsilon 1})}, \tag{20}$$

which suggests a better consistency of the new HTLES formulation (12, 18). The analytical derivation is detailed for the k-ε model in Appendix 7.1 using the less restrictive assumptions, i.e., inhomogeneous turbulence in a straight duct flow without assuming a constant ε_m. It is worth noting that $\psi(1) = 1$ when $r = 1$ in RANS mode, $\psi(r)$ increases when r is reduced in LES mode, and its maximum is reached when r goes to 0 at the DNS limit: $\psi(0) = C_{\varepsilon 2}/C_{\varepsilon 1}$.

At this point, the importance of the H-Equivalence criterion [16] is well supported. Without this criterion, it would have been impossible to analytically determine the expression of the hybridization function $\psi(r)$, while benefiting from the solid development framework of the TPITM [15]. This ultimately provides a hybrid approach whose transported variables are well identified, notably the second transported variable ε^*_m, and for which the RANS-to-LES transition is driven by a function exempt from empiricism.

3.4 Evaluation of the energy ratio related to the cutoff frequency

As proposed by Manceau [30], the HTLES model can be explicitly related to the temporal filter width, if r is analytically evaluated based on the cutoff frequency ω_c of the filter. Assuming that ω_c is in the inertial range of an equilibrium Eulerian spectrum, and according to Eq. (15), the energy ratio r_K (κ states for Kolmogorov) can be evaluated [30] as

$$r_K = \frac{k_m}{k} = \frac{1}{k}\int_{\omega_c}^{\infty} E_T(\omega)d\omega = \frac{1}{\beta_0}\left(\frac{U_s}{\sqrt{k}}\right)^{2/3}\left(\omega_c \frac{k}{\varepsilon}\right)^{-2/3}, \tag{21}$$

with $\beta_0 = 2/(3C_K)$. This relation involves the sweeping velocity U_s, the total energy k, and the total dissipation rate estimated as $\varepsilon = \varepsilon_m = \psi(r)\varepsilon^*_m$ (Eq. 17), considering that the resolved dissipation is negligible for ω_c in the inertial range.

The cutoff frequency is linked to the Nyquist frequency π/dt imposed by the time step dt. However, the cutoff frequency also depends on the grid step Δ, since for a sufficiently small time step the smallest vortices are filtered out by the grid, characterized by the spatial cutoff wavenumber $\kappa_c = \pi/\Delta$, and the relation between the cutoff frequency and the cutoff wavenumber, $\omega_c = U_s\kappa_c$, is driven by the sweeping mechanism, introduced by Tennekes [48], as recalled in section 3.2. Indeed, the characteristic frequency measured at a fixed point (Eulerian description) is not related to the eddy turnover time (Lagrangian time scale) of the eddies, but rather to the advection (sweeping) of the eddies by the large scales, as illustrated by Fig. 2. The left part of the figure shows the velocity signals measured at a fixed point generated by the advection of the blue and red eddies by the integral scale eddy. The characteristic frequency generated by these eddies is related to the sweeping velocity which, in the absence of average velocity, is written $U_s = \gamma\sqrt{k}$. The right part of the figure, which represents an Eulerian frequency spectrum, illustrates the fact that the grid step is at the origin of a cutoff frequency $\omega_c = U_s\pi/\Delta$: the characteristic frequency ω_2, related to the red eddy which is too small to be resolved, is missing in the frequency spectrum, in contrast to the frequency ω_1 related to the blue eddy.

Consequently, the highest resolvable frequency is the combination of the two cutoff frequencies

$$\omega_c = \min\left[\frac{\pi}{dt}, \frac{U_s\pi}{\Delta}\right], \tag{22}$$

in which, to also take into account the advection by the mean flow, U_s will be evaluated by $U_s = U + \gamma\sqrt{k}$, with U the mean velocity magnitude. For the usual case of a time step constant in the domain, the first component of expression (22) will be constant, and may activate in regions where the mesh is fine and/or the sweeping velocity is large. If the sweeping CFL number $U_s dt/\Delta$ is small enough, ω_c is imposed everywhere in the domain by the grid step, and Eq. (21) reduces to

$$r_K = \frac{1}{\beta_0}\left(\frac{\pi}{\Delta}\frac{k^{3/2}}{\varepsilon}\right)^{-2/3}, \tag{23}$$

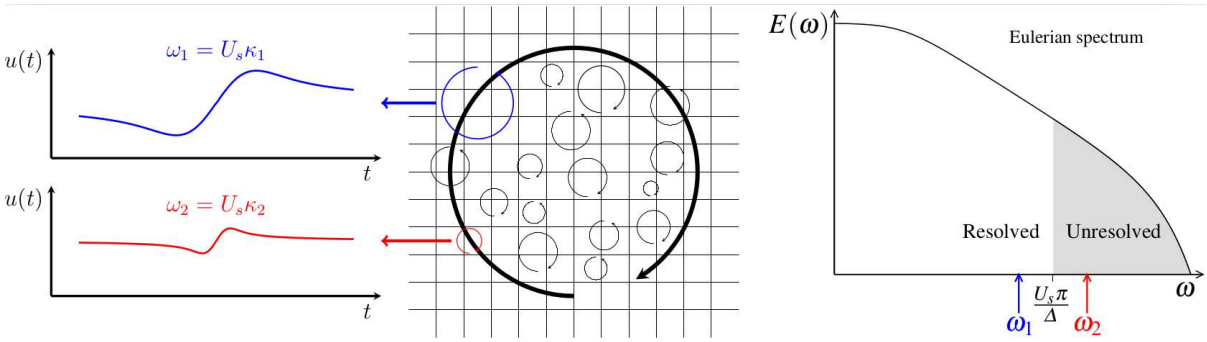

Fig. 2 Illustration of the sweeping mechanism of Tennekes [48] and its implications on the link between the cutoff frequency and the grid step. Middle: schematic view of eddies of various sizes present in a turbulent flow and the mesh used to try to resolve them. Left: Illustration of the temporal velocity signals measured at a fixed point due to the advection (sweeping) of the blue (resolved) and red (unresolved) eddies by the large-scale eddy, respectively. Right: Illustration of the Eulerian time spectrum and the position of the frequencies induced by these two eddies with respect to the cutoff frequency $U_s\pi/\Delta$.

which is the same expression as used by the PITM, which shows the consistency between the spatial and temporal approaches.

Note that the spatial filter width Δ is herein defined as the cubic root of the cell volume $\Omega^{1/3}$ to stay in line with the usual practice in LES.

3.5 Introduction of the turbulent time scale in the formulation

Following the original development of the HTLES model by Manceau [30], it is chosen to sensitize the model to the filter width via the introduction of the modeled time scale $T_\mathrm{m} = k_\mathrm{m}/\varepsilon_\mathrm{m}$, such that the dissipation term in the k_m-equation (12) is expressed as $\psi(r)\varepsilon^*_\mathrm{m} = k_\mathrm{m}/T_\mathrm{m}$, leading to

$$T_\mathrm{m} = \frac{r}{\psi(r)}\frac{k}{\varepsilon^*_\mathrm{m}}. \tag{24}$$

In the previous section, the theoretical analysis was conducted considering averaged quantities, such as $k_m = \overline{k_\mathrm{sfs}}$ and $\varepsilon^*_\mathrm{m} = \overline{\varepsilon^*_\mathrm{sfs}}$. However, it is the time-dependent equations of k_sfs and $\varepsilon^*_\mathrm{sfs}$ that must be solved in a hybrid RANS-LES model. Chaouat and Schiestel [10] and Fadai-Ghotbi *et al.* [14] have shown that the control of the level of modeled energy by the variation of the coefficients operates in the same way in these time dependent equations as in the averaged equations. Therefore, in the new formulation of HTLES, the subfilter viscosity ν_sfs and transport equations for k_sfs and $\varepsilon^*_\mathrm{sfs}$ are written as

$$\nu_\mathrm{sfs} = C_\mu \frac{k^2_\mathrm{sfs}}{\psi(r)\varepsilon^*_\mathrm{sfs}}, \qquad \begin{cases} \dfrac{Dk_\mathrm{sfs}}{Dt} = P_\mathrm{sfs} + D_{k\mathrm{sfs}} - \dfrac{k_\mathrm{sfs}}{T_\mathrm{m}}, \\ \dfrac{D\varepsilon^*_\mathrm{sfs}}{Dt} = C_{\varepsilon 1}\dfrac{\varepsilon^*_\mathrm{sfs}}{k_\mathrm{sfs}}P_\mathrm{sfs} + D^*_{\varepsilon\mathrm{sfs}} - C_{\varepsilon 2}\dfrac{{\varepsilon^*_\mathrm{sfs}}^2}{k_\mathrm{sfs}}. \end{cases} \tag{25}$$

The differences with the original formulation of HTLES lie in the expression of the hybridization function $\psi(r)$ (Eq. 20) and the presence of $\psi(r)$ in the subfilter viscosity formulation.

To evaluate the limiting form that this model takes in RANS mode, note that when the cutoff frequency goes to zero, the consistency of the filtering operator implies that the filtered quantities tend to their statistically-averaged counterparts, i.e. $k_\mathrm{sfs} = k_\mathrm{m} = k$, such that $r = 1$. Consequently, $\psi(1) = 1$, and according to equation (17), it leads to $\varepsilon^*_\mathrm{sfs} = \varepsilon^*_\mathrm{m} = \varepsilon_\mathrm{m} = \varepsilon$. Hence, the HTLES equations (25) tend to the standard equations of the k–ε RANS model

$$\nu_\mathrm{m} = C_\mu \frac{k^2}{\varepsilon}, \qquad \begin{cases} \dfrac{Dk}{Dt} = P + D_k - \varepsilon, \\ \dfrac{D\varepsilon}{Dt} = C_{\varepsilon 1}\dfrac{\varepsilon}{k}P + D_\varepsilon - C_{\varepsilon 2}\dfrac{\varepsilon^2}{k}. \end{cases} \tag{26}$$

In LES mode, the cutoff frequency ω_c is located in the inertial range of the turbulent spectrum, which means that the energy ratio r is lower than 1. It is simple algebra to show that $\psi(r)$ and the ratio $r/\psi(r)$ are decreasing and increasing functions of $r \in [0,1]$, respectively. Therefore, when the energy ratio r decreases, the time scale T_m (Eq. 24) is reduced. Hence, the destruction term of the k_sfs-equation (25) increases, corresponding to a reduction of the level of subfilter energy. In turn, the subfilter viscosity is reduced, which is expected in order to switch to the LES mode.

Finally, attention is focused on the decrease of the modeled viscosity ν_m when the filter width is reduced in LES mode. To do so, we can reduce the size of the filter by decreasing at the same time the time step and the grid step, by imposing $\Delta = U_s\,dt$, such that $\omega_c = \pi/dt = U_s\pi/\Delta$. We will then express the modeled viscosity as a function of Δ, in order to highlight the similarity with usual LES models. Hence, the energy ratio r (Eq. 21) reads

$$r_K = \frac{1}{\beta_0}\left(\frac{U_s}{\sqrt{k}}\right)^{2/3}\left(\frac{U_s\pi}{\Delta}\frac{k}{\psi(r)\varepsilon_{\mathrm{m}}^*}\right)^{-2/3} = \frac{1}{\beta_0\pi^{2/3}}\psi(r)^{2/3}\frac{{\varepsilon_{\mathrm{m}}^*}^{2/3}}{k}\Delta^{2/3}. \tag{27}$$

The modeled velocity ν_{m} (Eq. 18) is given by

$$\nu_{\mathrm{m}} = C_\mu\frac{{k_{\mathrm{m}}}^2}{\psi(r)\varepsilon_{\mathrm{m}}^*} = C_\mu\frac{{r_K}^2k^2}{\psi(r)\varepsilon_{\mathrm{m}}^*} = \frac{C_\mu}{\beta_0^2\pi^{4/3}}\psi(r)^{1/3}{\varepsilon_{\mathrm{m}}^*}^{1/3}\Delta^{4/3}. \tag{28}$$

The scaling of the modeled viscosity with $\Delta^{4/3}$ is the same as the one obtained with the Smagorinsky model, which shows that the model works in a similar way to a standard LES model in this condition. At the DNS limit ($r \to 0$), given that $\psi(0) = C_{\varepsilon 2}/C_{\varepsilon 1}$ and $\varepsilon_{\mathrm{m}}^* < \varepsilon_{\mathrm{m}} \leq \varepsilon$, it can be seen that $\nu_{\mathrm{m}} \to 0$ when $\Delta \to 0$. This demonstrates that, as expected, the equations tend to the Navier-Stokes equations in the limit of very fine grid and time steps. However, as will be discussed in section 4.2, in order to avoid the major issues of modeled-stress depletion and grid-induced separation [44], it is necessary to prevent the activation of the LES mode in the near-wall region. A shielding function will therefore be introduced to force the RANS mode up to about $y^+ = 100$, with the side effect that the model will no longer tend towards DNS in wall-bounded flows when the mesh is refined.

3.6 HTLES formulation applied to the k–ω SST closure

In the previous sections, the HTLES method has been applied to the k–ε model, because this model is the best candidate to illustrate and detail the derivation of the hybrid approach. However, the standard k-ε model is not valid in the near-wall region and requires some modifications, such as damping functions, to be extended to the wall. Such low-Reynolds-number k-ε models are not widely spread in the industry. One of the most popular approach is the k–ω SST model [33], which is a k-ε model extended to the wall by locally switching to the k-ω model. The HTLES is developed herein based on this particular closure. In the following, we show that the derivation of the k–ω SST HTLES model can be achieved in two ways.

First, the k–ω SST HTLES formulation can be derived by introducing a change of variable in the k–ε HTLES equations (25), in the same way as for the k–ω SST RANS models. The main benefit of this way of proceeding is that the expression of the hybridization function $\psi(r)$ (Eq. 20) is preserved irrespective of the closure. However, this derivation implies that the coefficient in the destruction term of the second transport equation is defined as $\beta_\omega = C_\mu(C_{\varepsilon 1} - \psi(r))$ (for the RANS derivation $\psi(r)$ is replaced by a coefficient equal to 1). In this regard, the second transport equation involves an additional term dependent on the hybridization function $\psi(r)$, which increases the complexity of the model formulation. Therefore, an alternative method is preferred.

The second way of deriving the k–ω SST HTLES formulation is to conduct the same perturbation analysis as for the derivation of the k–ε HTLES. We propose here to ensure H-equivalence with the k–ω SST TPITM developed by Bentaleb *et al.* [5], such that the hybridization function is transferred in the k_{m}-equation and a new variable transported by the second equation ω_{m}^* is introduced. The analysis is detailed in appendix 7.2, leading to a new hybridization function

$$\psi'(r) = \frac{\beta_\omega}{C_\mu\gamma_\omega + r(\beta_\omega - C_\mu\gamma_\omega)}, \tag{29}$$

where $\gamma_\omega = C_{\varepsilon 1} - 1$ and $\beta_\omega = C_\mu(C_{\varepsilon 2} - 1)$ are the usual coefficients of the RANS model. A clear similarity is observed between the hybridization functions $\psi(r)$ (Eq. 20) and $\psi'(r)$ (Eq. 29), using a k–ε and a k–ω SST closure, respectively. Finally, within the HTLES framework, the modeled time scale T_{m} (Eq. 24) is introduced, and the subfilter equations for ν_{sfs}, k_{sfs} and ω_{sfs}^* are written as

$$\nu_{\mathrm{sfs}} = \frac{k_{\mathrm{sfs}}}{\psi'(r)\omega_{\mathrm{sfs}}^*}, \qquad \begin{cases} \dfrac{Dk_{\mathrm{sfs}}}{Dt} = P_{\mathrm{sfs}} + D_{k\mathrm{sfs}} - \dfrac{k_{\mathrm{sfs}}}{T_{\mathrm{m}}}, \\ \dfrac{D\omega_{\mathrm{sfs}}^*}{Dt} = \gamma_\omega\dfrac{\omega_{\mathrm{sfs}}^*}{k_{\mathrm{sfs}}}P_{\mathrm{sfs}} + D_{\omega\mathrm{sfs}}^* - \beta_\omega{\omega_{\mathrm{sfs}}^*}^2 + C_{\omega\mathrm{sfs}}^*, \end{cases} \tag{30}$$

where $D_{\omega\mathrm{sfs}}^*$ stands for the diffusion of ω_{sfs}^*, and $C_{\omega\mathrm{sfs}}^*$ is the cross-diffusion term. The modeled time scale is evaluated as

$$T_{\mathrm{m}} = \frac{r}{\psi'(r)}\frac{k}{C_\mu k_{\mathrm{m}}\omega_{\mathrm{m}}^*}. \tag{31}$$

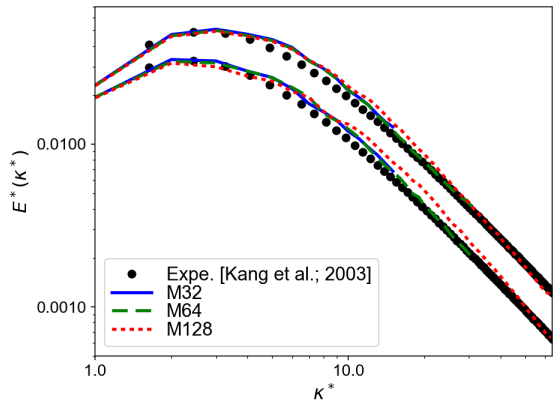

Fig. 3 Evolution of the resolved-energy spectra at two times. Reference data and k–ε HTLES results on 3 grids (M32, M64, M128) with $\beta_0 = 0.44$.

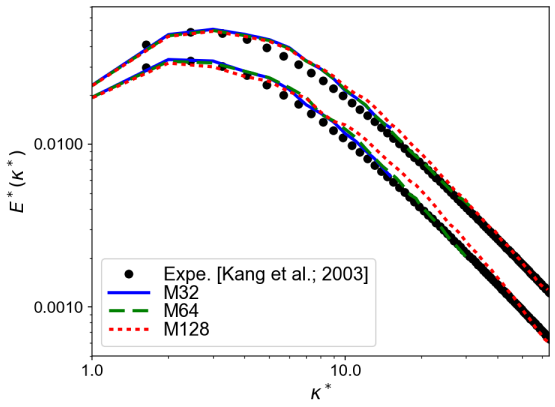

Fig. 4 Evolution of the resolved-energy spectra at two times. Reference data and k–ω SST HTLES results on 3 grids (M32, M64, M128) with $\beta_0 = 0.48$.

The complete formulation of the k–ω SST HTLES model is summarized in Appendix 7.3, including the limiters in the subfilter viscosity and production terms, as well as the blending functions of the RANS model of Menter [33].

3.7 Decaying Isotropic Turbulence

The coefficient $\beta_0 = 2/(3C_K)$ in Eq. (21) is provided by the theory as a function of the Kolmogorov coefficient C_K. Since the energy ratio r computed by Eq. (21) controls the level of resolved energy and eventually the subfilter viscosity, a computational verification against a database of isotropic turbulence is desirable to ensure that the hybrid model exhibits the correct level of subfilter dissipation within the context of particular models and numerical schemes. In this regard, the decaying isotropic turbulence (DIT) is a fundamental test case to evaluate the LES mode of HTLES and to assess the prediction of the energy cascade. The reference DIT data of Kang *et al.* [26] at $Re_\lambda = 720$ is used herein. Experimental data were recorded at four positions downstream of the grid, characterized by the grid step M. Calculations are performed within a triply-periodic cubic domain, focusing on the temporal decay of the isotropic turbulence in the fixed box. The initial velocity field is computed to match the energy spectrum at $x/M = 20$, as explained in [26], and the initial field of the turbulent variables are obtained by performing a frozen velocity field computation.

The computations are carried out using the k–ε HTLES and the k–ω SST HTLES implemented in code_saturne, a general CFD solver developed by EDF [3]. Since the hybrid model works in LES mode, the Crank-Nicholson time scheme and a spatial second-order centered scheme are used for the velocity (additional information on the CFD solver are given in section 5.1). In this homogeneous case, statistically-averaged quantities are evaluated using spatial averaging over the domain.

Fig. 3 and 4 show the resolved-energy spectrum at two times, corresponding to $x/M = 30$ and $x/M = 48$. In each case, 3 isotropic hexahedral meshes are used to assess the robustness of the model regarding grid refinement: M32, M64 and M128 with 32^3, 64^3 and 128^3 cells, respectively. The experimental results of [26] are used for comparison. A sensitivity study to the coefficient β_0 is performed in order to evaluate the prediction of the energy cascade, ensuring that the lack of resolved dissipative scales is compensated for by the subfilter dissipation. The best predictions are obtained with $\beta_0 = 0.44$ with k–ε and $\beta_0 = 0.48$ with k–ω SST (higher or lower values leading respectively to a lack or an excess of dissipation). It is remarkable that these values are very close to the theoretical definition of $\beta_0 = 2/(3C_K) = 0.44$. The slight discrepancy with the theoretical value for the k–ω SST model can be related to the fact that the ω-equation is not the exact equivalent of the ε-equation by change of variable, and the value $\beta_0 = 0.48$ will be used in the subsequent computations. These results show that the slight adaptation of the coefficient driving the LES branch of HTLES is essential to get similar predictions irrespective of the closure. Although this test in DIT does not guaranty that the LES branch of the hybrid model will work properly for all the configurations, it is fundamental to prove that the model indeed provides the correct level of subfilter dissipation [49].

4 Improvement of the HTLES model for wall-bounded flows

This section is devoted to the improvement of HTLES in channel flows. The developments are henceforth based on the k–ω SST model, since the use of a low-Reynolds-number model is relevant to focus on the near-wall region. The

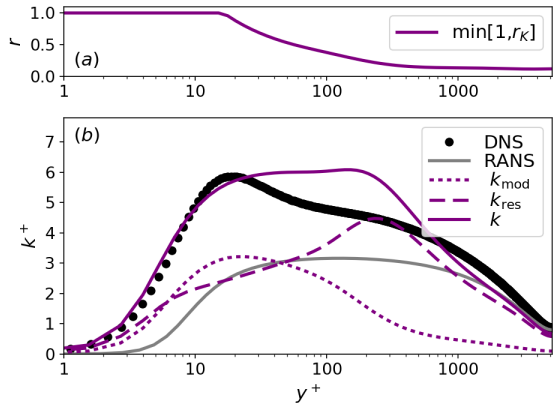

Fig. 5 Energy ratio (a) and kinetic energy profiles (b). HTLES model (without ICC). Channel flow at $Re_\tau = 5200$.

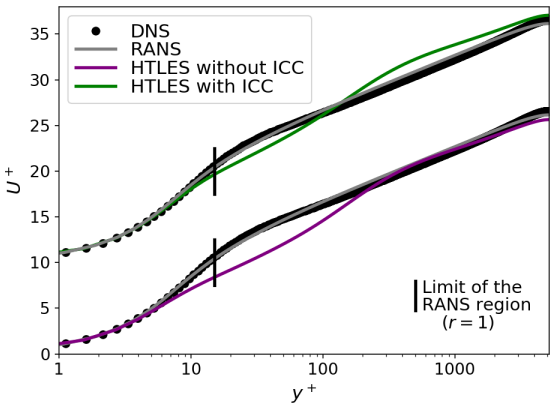

Fig. 6 Mean velocity profiles. HTLES without ICC and HTLES with ICC. Channel flow at $Re_\tau = 5200$.

behavior of HTLES in this zone is indeed a major concern, since the transition from RANS to LES occurs in this region in most hybrid approaches. The main results are illustrated using the case of the plane channel flow at Reynolds number $Re_\tau = 5200$ compared to the reference DNS by Lee and Moser [29]. The k–ω SST HTLES calculations are performed using code_saturne (see section 5.1), and grid C1 is defined in Table 1, based on the common practice for hybrid approaches. Extensive validation over a range of grids and Reynolds numbers is carried out in section 5.

Table 1 Grid for the channel flow with half-width δ in the domain $L_x \times L_y \times L_z = 6.4\delta \times 2\delta \times 3.2\delta$.

Re_τ	Grid	Δ_x^+	Δ_z^+	$\Delta_{y_c}^+$	$\Delta_{y_w}^+$	Δ_x/δ	Δ_z/δ	N_x	N_y	N_z
5200	C1	520	260	260	1	0.1	0.05	64	140	64

4.1 Consistency with the RANS model

In wall-bounded flows, the first concern is that the estimation of the energy ratio with Eq. (21) can lead to unrealistic values larger than unity, since the Kolmogorov assumption is not relevant in the viscous wall region. To address that problem, Tran *et al.* [49] introduced an upper bound in the definition of the energy ratio, resulting in $r = \min[1, r_K]$. For this particular mesh, Fig. 5a shows that the energy ratio is equal to one in the near-wall region below $y^+ = 15$, which means that this zone is treated in RANS mode, before decreasing and reaching a plateau ($r \simeq 0.12$) in the LES region.

By analysing the energy partition in Fig. 5b, it is observed that the resolved energy k_r is not zero in the RANS region as it should be in theory. Resolved fluctuations coming from the outer LES region penetrate into the near-wall RANS region, which leads to an inconsistency, since the model is built assuming that the resolved energy is zero in RANS mode. Hence, the total energy $k = k_r + k_m$ is overestimated compared to the RANS solution $k = k_m$, such that the time scale T_m defined by Eq. (31) is overestimated and the destruction term of the energy equation (30) is too low compared to the RANS formulation. As shown in Fig. 6, this issue results in an underestimation of the HTLES velocity profile in the RANS region, although it is expected that the HTLES tends to the RANS solution. This problem causes large discrepancies all over the RANS-to-LES transition region.

To address this issue, an internal consistency constraint (ICC) is defined herein. The coefficient c_r is added in the definition of the turbulent time scale, in order to recover the exact formulation of the RANS closure when $r = 1$,

$$T_m = \frac{r}{\psi'(r)} \frac{k_m + c_r k_r}{C_\mu k_m \omega_m^*}, \qquad \text{where } c_r = \begin{cases} 0 \text{ if } r = 1, \\ 1 \text{ if } r < 1. \end{cases} \tag{32}$$

Using the ICC, Fig. 6 shows that the solution of the RANS model is much better recovered throughout the region where $r = 1$. However, the ICC does not improve the discrepant results in the transition and LES regions, which are related to the location of the RANS-to-LES switch, as explained in the following section.

4.2 Control of the RANS-to-LES transition in the near-wall region

The RANS-to-LES transition of the model must be imposed with the objective of significantly reducing the number of grid cells in the near-wall region compared to LES. To this end, it is relevant to analyse the behavior of the energy ratio in the log layer. In this region, the equality $C_\mu^{3/4} k^{3/2}/\varepsilon = C_\kappa d_w$ is satisfied [36], where C_κ is the Van Karman constant and d_w the distance to the wall. Hence, when the cutoff frequency of the filter is related to the grid step (i.e. $\omega_c = U_s \pi/\Delta$), we show that the energy ratio (Eq. 21) can be evaluated as

$$r_K = \frac{C_\mu^{1/2}}{\beta_0 \pi^{2/3} C_\kappa^{2/3}} \left(\frac{\Delta}{d_w}\right)^{2/3}. \tag{33}$$

One observes that the energy ratio is only dependent on the grid step, irrespective of the Reynolds number. It decreases with the distance to the wall, and this decrease encompasses the entire log layer. This observation is in line with the hybridization strategy which is adopted to treat the different wall regions of a turbulent boundary layer [36]: the RANS mode is enforced in the viscous and buffer sublayers, the transition takes place in the log layer, and rest of the outer layer is treated in LES mode.

However, using the present formulation, the RANS-to-LES transition can occur too close to the wall, since the energy ratio $r = \min[1, r_K]$ is dependent on the grid step. Notably, using grid C1, Fig. 5 shows that the transition occurs in the buffer layer. This issue has been encountered in many hybrid approaches, leading to modeled-stress depletion and grid-induced separation, as shown by Spalart *et al.* [47]. This issue has already been addressed by introducing a shielding function to enforce the RANS mode in the near-wall region, such as the DDES shielding [47] or the shielding based on elliptic blending proposed by Fadai-Ghotbi *et al.* [15] within the TPITM context. Following [15], the energy ratio is defined as a blending between its usual definition and unity,

$$r = (1 - f_s) \times 1 + f_s \times \min[1, r_K], \tag{34}$$

introducing a new shielding function f_s. Although, unfortunately, the introduction of such a shielding function reintroduces into the model a dose of empiricism that the theoretical formalism aims at suppressing, it is necessary in order to avoid a deterioration of the results when ambiguous near-wall meshes are used (fine enough to resolve turbulent structures but too coarse to perform a wall-resolved LES). The definition of f_s is a major concern, as during its transition from 0 in the near-wall region to 1 far from the wall, it directly impacts the decreasing trend of the energy ratio. In particular, since it is necessary to prevent the model from switching to LES mode when the mesh is ambiguous, the spatial extension of the shielding must be independent of the grid. The following section is dedicated to the development of such a function.

4.2.1 A grid-independent shielding of the viscous wall region

The new shielding function f_s is built to provide a constant shielding of the near-wall region, irrespective of the model or the numerical parameters. Notably, following the previous remarks (deduced from expression 33), the main objective is to enforce the RANS mode in the viscous wall region, where the LES mode is not desirable, aiming at satisfying the constraints below:

(i) The RANS mode extends up to the log layer.
(ii) The shielding function involves a quite sharp transition at the beginning of the log layer in order to recover the decreasing trend defined by Eq. (33).
(iii) The shielding function is independent of grid refinement.
(iv) The shielding function is independent of the closure, to develop a global shielding function, not specifically related to a RANS model or a hybrid method.

For this purpose, a dimensionless scale ratio is introduced, using a hyperbolic tangent function to provide a continuous transition from 0 to 1. To ensure the grid independency of the ratio, the comparison is based on the distance to the wall and a turbulent length scale. Since, as mentioned above, resolved dissipation is negligible, the modeled dissipation rate is equal to the total dissipation ε and is therefore independent of the grid. Therefore, the Kolmogorov length scale is a good candidate for defining a grid-independent shielding, in the form

$$f_s(\xi_K) = 1 - \tanh\left[\xi_K^{p_1}\right], \qquad \text{where} \quad \xi_K = C_1 \frac{(\nu^3/\varepsilon)^{1/4}}{d_w}, \tag{35}$$

with the coefficients C_1 and p_1. Note that in the log layer, the length scale ratio ξ_K can be estimated using the standard relation $\varepsilon^+ = 1/(C_\kappa y^+)$ in wall units, such that

$$\xi_{K\log} = C_1 C_\kappa^{1/4} y^{+-3/4} \tag{36}$$

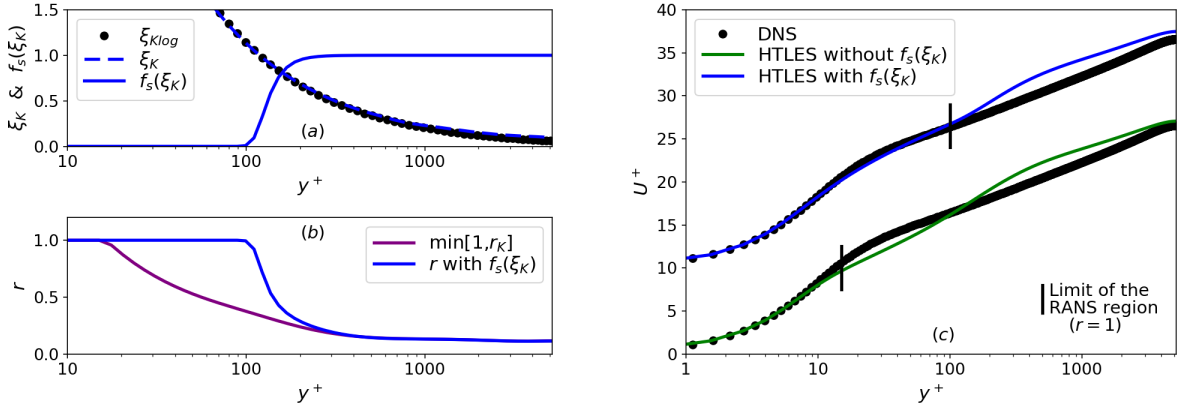

Fig. 7 Profiles of the shielding functions (a), the energy ratios (b) and the mean velocities (c). HTLES model with ICC, with and without the shielding function $f_s(\xi_K)$. Channel flow at $Re_\tau = 5200$.

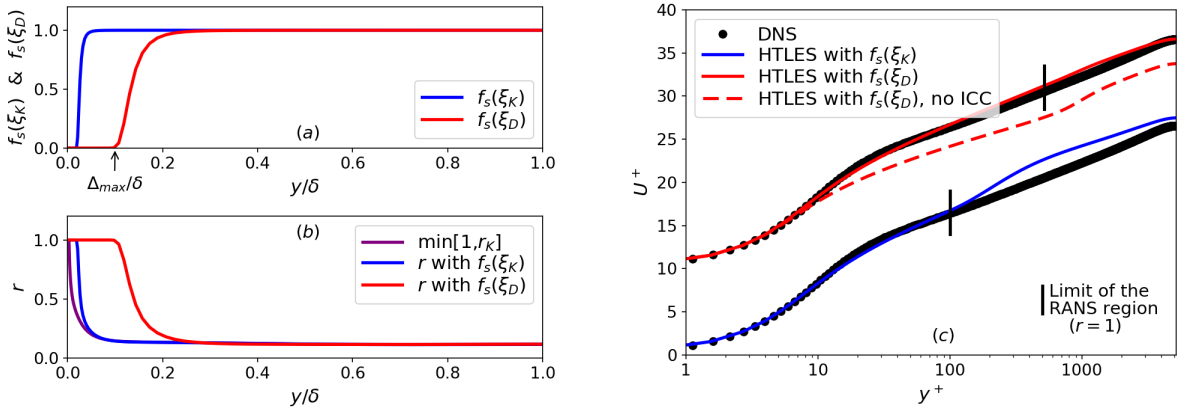

Fig. 8 Profiles of the shielding functions (a), the energy ratios (b) and the mean velocities (c). HTLES with ICC, with $f_s(\xi_K)$ or $f_s(\xi_D)$. Channel flow at $Re_\tau = 5200$.

in this region. The expected behavior of the length scale ratio ξ_K is obtained: it goes to infinity at the wall and zero away from the the wall, and it is independent of the grid step and the model. The analytical relation (36) is useful for calibrating coefficients C_1 and p_1, providing an accurate setting of the location and the sharpness of the transition region. Following the previous specifications (i) and (ii), it seems relevant to enforce the RANS-to-LES switch at the beginning of the log layer. In that respect, it has been chosen on the basis of a sensitivity study for several Reynolds numbers between 590 and 20000 (not shown here) to extend the RANS region up to $y^+ = 100$, and to impose a relatively sharp transition between $y^+ = 100$ and 200. The calibration of the coefficients, based on Eq. (36), leads to $C_1 = 45$ and $p_1 = 8$ (the sensitivity study showed that the results are not sensitive to small variations of these values).

Fig. 7a shows that the length scale ratio ξ_K (Eq. 35) computed during the calculation matches $\xi_{K\log}$ (Eq. 36) in the log layer. Hence, the shielding function $f_s(\xi_K)$ imposes the desired transition region. In Fig. 7b, applying the shielding function, it is verified that the RANS mode ($r = 1$) is enforced up to $y^+ = 100$. In the transition region, the decreasing trend of the energy ratio is related to the slope of the shielding function until $y^+ = 200$, and the behavior of r_K (Eq. 21) is recovered beyond this location.

Finally, Fig. 7c shows the velocity profile obtained using HTLES with the shielding function $f_s(\xi_K)$. The internal consistency constraint (Eq. 32) is modified by introducing

$$c_r = \begin{cases} 0 \text{ if } r = 1, \\ f_s \text{ if } r < 1, \end{cases} \tag{37}$$

in order to provide a continuous correction of the time scale T_m. On the one hand, the RANS behavior is correctly recovered in the near-wall region up to $y^+ = 100$, as desired. On the other hand, in the LES region, an overestimation of the velocity profile is observed, corresponding to the so-called log-layer mismatch [35], which is tackled in the following section.

4.2.2 A grid-dependent shielding to address the log-layer mismatch

The log-layer mismatch observed in Fig. 7c has been encountered in many hybrid approaches since the study of Nikitin *et al.* [35]. It consists of a shift of the logarithmic profile originating in the transition region, such that the velocity is overestimated in the LES region. Some proposals have already been made to address this issue, using an additional shielding function in IDDES by Shur *et al.* [42] or applying forcing techniques as discussed by Keating and Piomelli [27]. Actually, the log-layer mismatch is due to a switch from RANS to LES in a region where the cells are not adequate to properly resolve the turbulent fluctuations. In the case of the present model, the energy ratio (Eq. 21) depends on the grid step evaluated as the cubic root of the volume of the cell, which can lead to a switch to LES in a region where the grid is very coarse in streamwise or spanwise directions.

In that respect, a relevant scale is the maximum dimension of the cell $\Delta_{\max} = \max[\Delta_x, \Delta_y, \Delta_z]$ in order to enforce the RANS mode where the mesh is too coarse in any of the directions. Notably, following the analysis of Larsson *et al.* [28] in WMLES, and Han *et al.* [21] in IDDES, it is pointed out that to properly capture the large-scale fluctuations in the near-wall region treated in LES mode, the integral length scale L must be at least greater than twice the maximum grid size (Nyquist theorem): $L \geq 2\Delta_{\max}$. In addition, L can be explicitly related to the distance to the wall d_w in the log layer [36]: $L = k^{3/2}/\varepsilon = C_\kappa / {C_\mu}^{3/4} d_w$. Based on these expressions, the following criterion is obtained to activate the LES mode in regions where the grid is fine enough in any of the directions for properly resolving the largest structures: $d_w \geq 0.8\Delta_{\max}$. Hence, to address the log-layer mismatch, we propose to introduce a second shielding function, dependent on a new ratio ξ_D. This ratio compares $\Delta_{\max}$ and d_w, in order to activate the LES mode from $\Delta_{\max} = d_w$ (satisfying the previous criterion with a small safety margin), such that

$$f_s(\xi_D) = 1 - \tanh\left[\xi_D^{p_2}\right], \qquad \text{where} \quad \xi_D = C_2 \frac{\Delta_{\max}}{d_w}. \tag{38}$$

The calibration of the coefficients C_2 and p_2 is done in order to ensure a similar sharpness for $f_s(\xi_K)$ and $f_s(\xi_D)$. ξ_K scales as ${d_w}^{-3/4}$ in the log layer according to Eq. (36). In the same way, ξ_D scales as ${d_w}^{-1}$, assuming that $\Delta_{\max}$ is constant (usual structured mesh). Since $p_1 = 8$, it is necessary to impose $p_2 = 6$ in order to provide the same decreasing trend for $\xi_K^{p_1}$ and $\xi_D^{p_2}$, with a calibrated coefficient $C_2 = 1.2$.

In Fig. 8a, it is verified that the switch of $f_s(\xi_D)$ occurs just after the location where $d_w = \Delta_{\max}$, as desired. Hence, using the mesh C1 defined in Table 1, the RANS mode is extended up to 0.1δ, as shown in Fig. 8b. It is noted that in the LES region, the energy ratio tends to the same value, regardless of the location or the sharpness of the transition region. The benefit of the new shielding function is clearly visible in Fig. 8c, showing the velocity profiles. A very satisfactory agreement with the reference data is obtained in the RANS mode, thanks to the ICC, as well as in the LES mode, since the RANS-to-LES transition occurs in a region where the cells are suitable to resolve the turbulent structures, using $f_s(\xi_D)$. In addition, Fig. 8c shows that the introduction of the ICC is essential to recover the correct RANS formulation when $r = 1$, notably when the RANS mode is enforced by the shielding functions.

It is important to highlight that, although the largest extent of the shielding is imposed by $f_s(\xi_D)$ for the present mesh, $f_s(\xi_K)$ is relevant to enforce the RANS mode up to $y^+ = 100$ in all the situations. Indeed, the grid-independent shielding function $f_s(\xi_K)$ ensures the robustness of the HTLES formulation when the grid is overly refined in the near-wall region, while the complementary shielding function $f_s(\xi_D)$ protects the regions where the cells are too anisotropic to properly resolve the turbulent structures.

Finally, the introduction of the two shielding functions is decisive, in order to properly control the RANS-to-LES transition in the vicinity of the wall. Associated with the ICC, these improvements are effective regarding the predictions of the velocity profiles, as shown successively in Fig. 6, 7 and 8. Despite involving some empiricism, arguments are presented to justify the need for these improvements, as well as to explain how a suitable location of the RANS-to-LES transition is established as a function of physical parameters ($f_s(\xi_K)$) and grid characteristics ($f_s(\xi_D)$). Once the RANS zone is sufficiently improved, the log-layer mismatch is largely erased. Extensive validation is continued in the next section on channel flows at various Reynolds numbers, using different grids, and the periodic-hill test case.

5 Validation of the HTLES approach

The validation process of the k–ω SST HTLES model is now carried out on channel and periodic-hill flows, including sensitivity study to the grid and the Reynolds number. The Cartesian coordinates x, y, z are aligned with the streamwise, wall-normal and spanwise directions, respectively. The global formulation of the k–ω SST HTLES model is summarized in Appendix 7.3, including the internal consistency constraint (Eq. 37) and the two-fold shielding function f_s (Eq. 35 and 38), which is written as follows

$$f_s(\xi_K, \xi_D) = 1 - \tanh\left[\max\left[\xi_K^{p_1}, \xi_D^{p_2}\right]\right]. \tag{39}$$

5.1 Numerical setup

The calculations are performed using code_saturne [3], the open-source CFD software developed by EDF and distributed under Gnu GPL license (https://www.code-saturne.org). The code is based on a finite-volume method, using a fully co-located arrangement for all the variables. The velocity-pressure system is solved using a standard predictor-corrector scheme (SIMPLEC).

The time-marching is based on a second-order accurate Crank-Nicholson scheme. A particular attention is paid to the convection scheme for the filtered velocity equation since the use of a centered scheme is a key requirement in LES mode but can lead to numerical instabilities in RANS mode. A hybrid scheme (HYB) similar to the one proposed by Travin *et al.* [50] is used: a second-order upwind scheme (SOLU) and a centered difference scheme (CDS) are blended using the coefficient c_r (Eq. 37) to be in line with the switch from RANS to LES, such that

$$\Phi_{\mathrm{HYB}} = (1 - c_r)\Phi_{\mathrm{SOLU}} + c_r \Phi_{\mathrm{CDS}}. \tag{40}$$

For the convection terms of the transport equations of the turbulent variables, a first order upwind scheme is applied to favour numerical stability, as these terms are less sensitive than for the momentum equation and can be discretized to a lower order [4, 11].

As a practical matter, during the calculations, an exponentially-weighted average [37] is used to estimate the statistically-averaged quantities (k_{r}, k_{m}, ω^*_{m}, ...). For the statistically stationary flows studied in this paper, the time filter width is chosen to correspond to several tens of flow-through times, ensuring the convergence of the statistical estimates. Note that, for non-stationary flows, Afailal [1] proposed a suitable estimation of the temporal filter width in the framework of HTLES, and the dynamic time filtering technique developed by Jamal and Walters [24] could also be used.

5.2 Channel flows

Channel flows are investigated to validate HTLES against DNS results at $Re_\tau = 590$ (Moser *et al.* [34]), $Re_\tau = 1000$ and 5200 (Lee and Moser [29]), and a RANS k–ω SST computation at $Re_\tau = 20000$, where $Re_\tau = u_\tau \delta / \nu$, δ is the channel half-width, u_τ is the friction velocity and ν is the kinematic viscosity.

Table 2 Numerical settings of the grids for the channel flows in domain $L_x \times L_y \times L_z = 6.4\delta \times 2\delta \times 3.2\delta$.

Re_τ	Grid	Δ_x^+	Δ_z^+	$\Delta_{y_c}^+$	$\Delta_{y_w}^+$	Δ_x/δ	Δ_z/δ	N_x	N_y	N_z
590	**A1**	60	30	30	1	0.1	0.05	64	96	64
1000	**B1**	100	50	50	1	0.1	0.05	64	106	64
5200	C0	260	130	260	1	0.05	0.025	128	140	128
	C1	520	260	260	1	0.1	0.05	64	140	64
	C2	1040	520	260	1	0.2	0.1	32	140	32
	C1X	260	260	260	1	0.05	0.05	128	140	64
	C2X	520	520	260	1	0.1	0.1	64	140	32
20000	**D1**	2000	1000	1000	1	0.1	0.05	64	166	64

Grids A1, B1, C1 and D1 defined in Table 2 are characterized by the same number of cells in the x and z-direction, respectively, i.e. by the same cell sizes: $\Delta_x = 0.1\delta$ and $\Delta_z = 0.05\delta$ are fixed regardless of the Reynolds number. In the wall-normal direction, $\Delta_{y_w}^+ = 1$ at the wall and the cell size increases up to $\Delta_{y_c} = 0.05\delta$ at the center of the channel. This meshing strategy corresponds to one of the main objectives of hybrid RANS-LES, which is to use a RANS type mesh in the near-wall region. It is strongly related to the introduction of the second shielding function $f_s(\xi_D)$ (Eq. 38), since the extent of the RANS region scales with the maximum cell dimension. The sensitivity study to the Reynolds number is carried out using these grids, which demonstrates that the scaling of the numerical cost drastically decreases compared to LES (in the x and z-direction, the cost reduction scales with Re_τ^2). Even if these grids are designed within a particular context, using specific models, numerical methods and software, it is worth noting that the resolution is close to the one used in most hybrid computations (see, e.g., the IDDES simulations of Shur *et al.* [42], among others), and to the streamwise and spanwise resolutions used for wall-modeled LES following the analysis of Larsson *et al.* [28]. In contrast, grids C0, C1, C2, C1X and C2X are designed to study the sensitivity to the mesh at $Re_\tau = 5200$. The differences between these grids lies in the grid steps and the aspect ratio in streamwise and spanwise directions, while the cell distribution in the wall-normal direction is preserved.

To begin with, in order to give a point of reference and evaluate the influence of the numerical method, no-model simulations (i.e. coarse DNS) are performed, using grids A1, B1, C1 and D1. In addition, the standard Smagorinsky

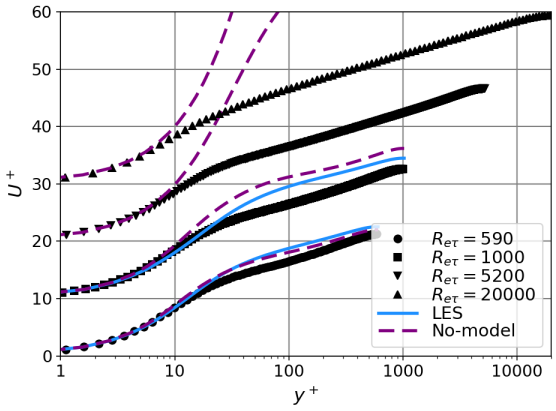

Fig. 9 Mean velocity profiles, channel flows for different Re. Smagorinsky LES and no-model simulations using grids A1, B1, C1 and D1.

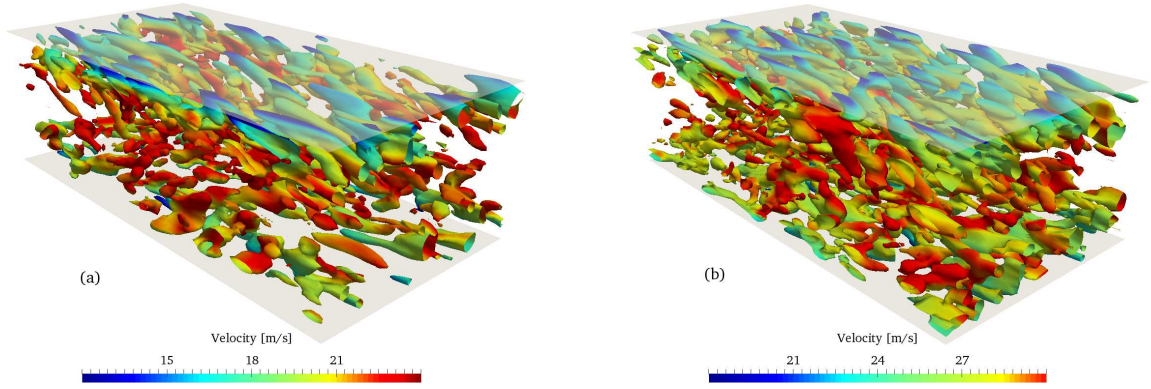

Fig. 10 Iso-surfaces of the Q-criterion ($Q = 50u_\tau^2/\delta^2$) colored by the velocity magnitude, channel flows at (a) $Re_\tau = 1000$ and (b) $Re_\tau = 20000$, HTLES calculation using grids B1 and D1, respectively.

model [43] ($\nu_{\text{sfs}} = (C_s\Delta)^2\widetilde{S}$ with C_s the usual coefficient) is used as a reference. As shown in Fig. 9, at low Reynolds numbers, the results are not so discrepant, given that the grid is relatively fine in wall-units ($\Delta_x^+ = 60$ and $\Delta_z^+ = 30$), but the overestimation of the velocity profiles is much more pronounced when increasing the Reynolds number (for $Re_\tau > 1000$, large non-physical instabilities are observed for the Smagorinsky LES model, and the results are not added in Fig. 9). These results demonstrate the relevance of the hybrid RANS-LES approach with a meshing strategy based on geometric criteria.

In Fig. 10, performing HTLES calculations, iso-surfaces of the Q-criterion at $Re_\tau = 1000$ and $Re_\tau = 20000$ show that large-scale turbulent structures are explicitly resolved in the core region of the flow. In this region, the LES mode of HTLES is activated, sustaining the resolved turbulence during the calculation. In contrast, in the very near-wall region treated in RANS mode, the turbulent structures are not visible, notably at moderate Reynolds number $Re_\tau = 1000$.

Considering the sensitivity to the Reynolds number, Fig. 11 shows that the velocity profiles are well predicted, in both RANS and LES mode (in contrast with no-model and LES predictions in Fig. 9). In particular, it is remarkable that the log-layer mismatch is erased over a large range of Reynolds numbers. These satisfactory results are notably due to the introduction of the ICC (Eq. 32 and 37) and the shielding functions (Eq. 35 and 38) in the HTLES model, as explained in section 4.

Fig. 12 shows the profiles for $f_s(\xi_K)$ and $f_s(\xi_D)$, as a function of the distance to the wall in wall units (left) or scaled with the half-width of the channel δ (right), in logarithmic or linear scales, respectively. As observed previously, $f_s(\xi_K)$ imposes a constant shielding in wall units, but at high Reynolds numbers the shielded region is not large enough. In contrast, the shielding function $f_s(\xi_D)$ imposes exactly the same transition region from 0.1δ to 0.2δ using standard grids, regardless of the Reynolds number. Even if the shielding function $f_s(\xi_K)$ is only active for Reynolds numbers lower than $Re_\tau = 1000$ herein (or, in more specific terms, using fine grids for which $\Delta^+_{\text{max}} \leq 100$), it is still a key requirement since a wide variety of grids and Reynolds numbers can be encountered in industrial applications.

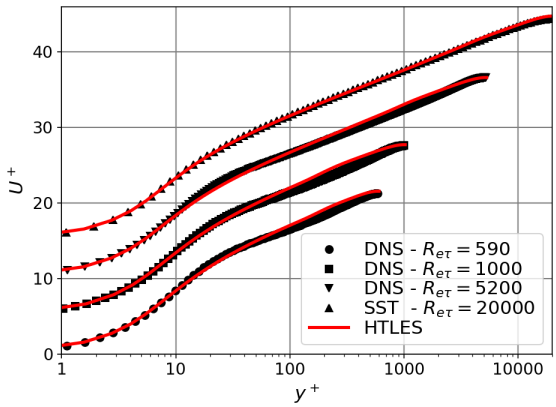

Fig. 11 Mean velocity profiles, channel flows for different *Re*. HTLES results, using grids A1, B1, C1 and D1.

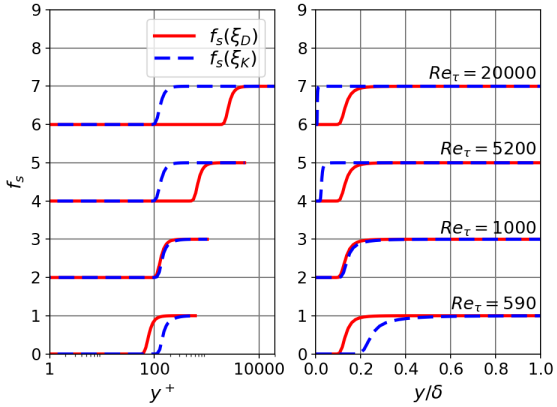

Fig. 12 Profiles of the shielding functions, channel flows for different *Re*. HTLES results, using grids A1, B1, C1 and D1.

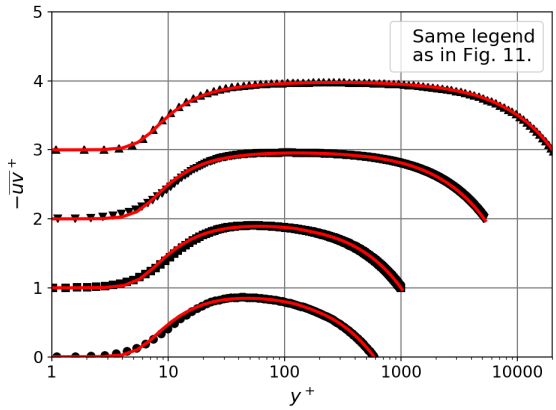

Fig. 13 Total shear stress profiles, channel flows for different *Re*. HTLES results, using grids A1, B1, C1 and D1.

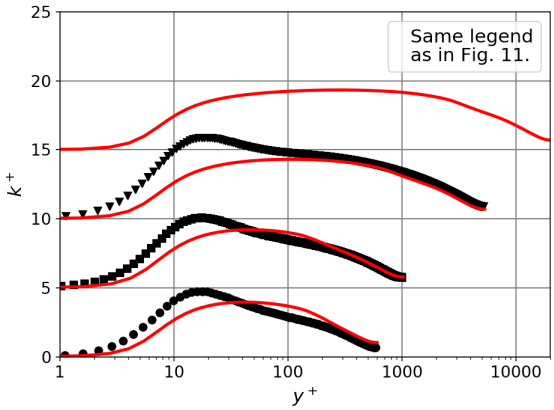

Fig. 14 Total kinetic energy profiles, channel flows for different *Re*. HTLES results, using grids A1, B1, C1 and D1.

Fig. 13 shows that the shear stress profiles closely match the reference data. Regarding the turbulent energy profiles in Fig. 14, noticeable discrepancies appear in the RANS region. As with all linear eddy-viscosity models, the underlying k–ω SST closure is calibrated to reproduce the shear-stress and mean velocity profiles, and is not well suited for properly predicting the turbulent energy in the vicinity of the wall. This behavior is inherited by the hybrid model in regions treated in RANS mode, as expected. Despite this weakness, the use of the RANS model at the wall is crucial when using grids for which LES and no-model simulations are severely discrepant (Fig. 9).

Now, the influence of the grid resolution is investigated. In Fig. 15a, it is verified that the shielding function $f_s(\xi_K)$ is independent of the grid, whereas the switch of the second shielding function $f_s(\xi_D)$ occurs when the distance to the wall is equal to the largest cell width ($\Delta^+_{\max} = 260$, 520 or 1040, respectively). In Fig. 15b, it can be seen that the location of the RANS-to-LES transition is dictated by the parameter ξ_D. A plateau is reached in the LES region, and as expected, the value of the energy ratio reached in this region decreases when the mesh is refined.

The way the grid resolution affects the accuracy is underlined by the velocity profiles in Fig. 16. HTLES results using grids C1X and C2X with the same grid steps in streamwise and spanwise directions show some discrepancies in the LES region. The log-layer mismatch is not fully reduced. In contrast, HTLES using grids C0, C1 and C2, characterized by cells elongated in the streamwise direction, show good predictions in both RANS and LES regions. Notably, it is observed that the results are far better using grid C1 rather than grid C1X, although C1X is refined in the streamwise direction (the same holds true for C2 and C2X, respectively). Indeed, using grids C1X and C2X, the extension of the shielding $f_s(\xi_D)$ is reduced by a factor of two (scaling with $\Delta_{\max}$), and the LES mode is activated closer to the wall, in a region where the turbulent structures are smaller. Consequently, the grid is not fine enough to properly capture these turbulent structures, in particular regarding the spanwise refinement, which is unchanged between C1 and C1X (C2 and C2X). These results suggest that the use of isotropic cells in the x and z-direction is not well suited for properly resolving the large-scale turbulent structures in the log-layer where the LES mode is activated. Some recommendations

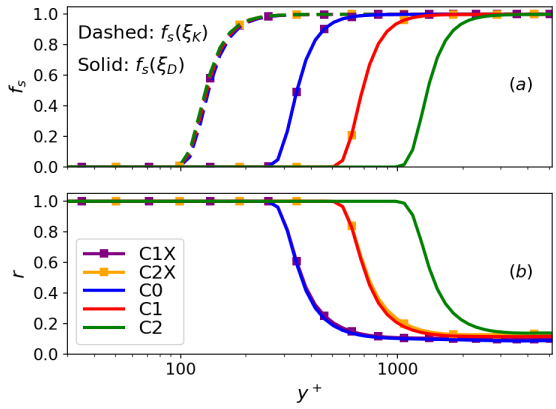

Fig. 15 Profiles of the shielding function (a) and the energy ratio (b), channel flow at $Re_\tau = 5200$. HTLES results, using grids C0, C1, C2, C1X and C2X, .

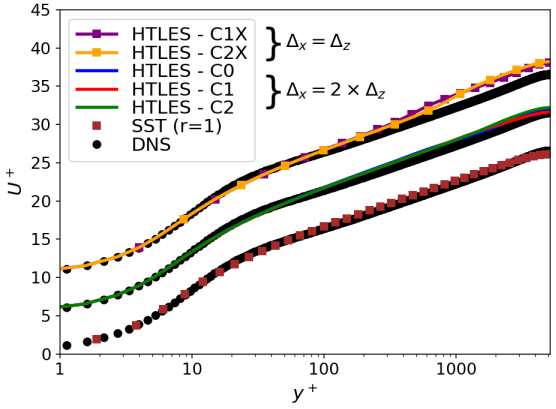

Fig. 16 Mean velocity profiles, channel flow at $Re_\tau = 5200$. HTLES results, using grids C0, C1, C2, C1X and C2X, and RANS k–ω SST results.

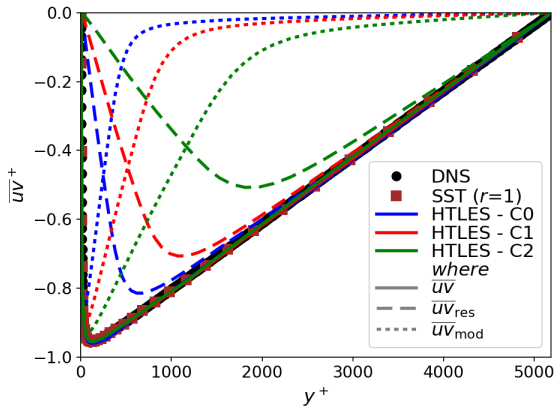

Fig. 17 Shear stress profiles, channel flow at $Re_\tau = 5200$. HTLES results, using grids C0, C1, C2, and RANS k–ω SST results.

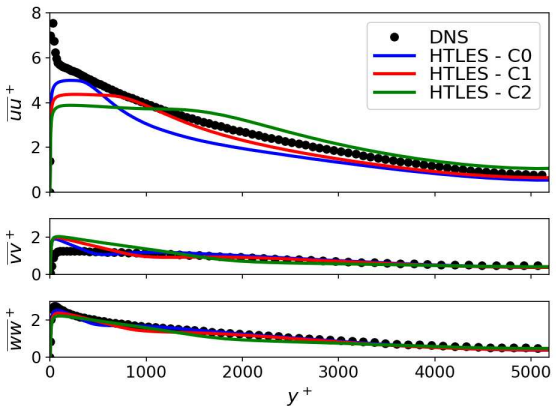

Fig. 18 Profiles of the total Reynolds stresses, channel flow at $Re_\tau = 5200$. HTLES results, using grids C0, C1 and C2

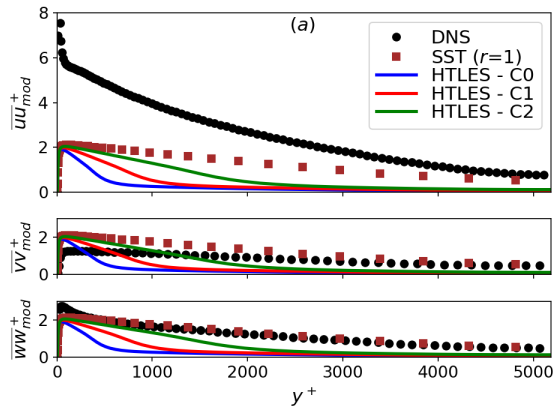

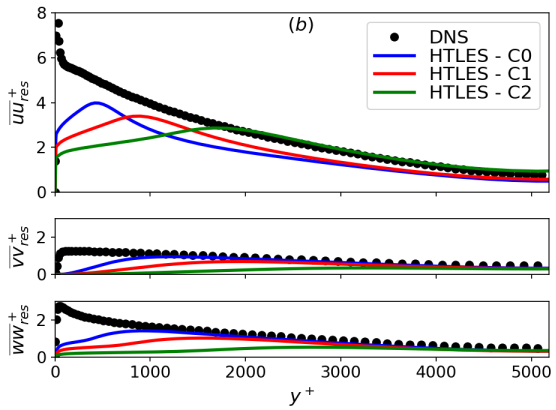

Fig. 19 Profiles of the modeled (a) and resolved (b) Reynolds stresses, channel flow at $Re_\tau = 5200$. HTLES results, using grids C0, C1 and C2, and RANS k-ω SST results (a).

are provided for the grid ($\Delta_x = 0.1\delta$, $\Delta_z = 0.05\delta$), which are consistent with the WMLES recommendations ($\Delta_x = 0.08\delta$, $\Delta_z = 0.05\delta$) by Larsson *et al.* [28]. Hence, beyond the grid refinement, the shape of the cells has an influence on the predictions as well.

Using grids C0, C1 and C2, the total shear stress matches the reference data perfectly in Fig. 17. The partition of energy among modeled and resolved scales fulfills the expected behavior of hybrid approaches: the modeled part is dominant in the near-wall region and is gradually replaced by the resolved part away from the wall; the contribution of the resolved part increases when the mesh is refined; and the location where it becomes larger than the modeled part gets closer to the wall.

In Fig. 18, it is shown that the anisotropic behavior of the total Reynolds stresses is satisfactorily reproduced in the LES region. The coarser mesh C2 leads to a slight overestimation of the streamwise fluctuations, since the cells are too large to properly resolve the turbulent fluctuations. In contrast, in the RANS region, noticeable discrepancies appear. As shown in Fig. 19, these discrepancies are mainly due to the underlying turbulence model, k–ω SST, based on the Boussinesq assumption. In particular, in the near-wall region where the RANS mode of HTLES is activated, the modeled stresses do not reflect the turbulence anisotropy. Regarding the resolved components, it is noted that resolved fluctuations penetrates into the near-wall RANS region, which improves the predictions for the total turbulent stresses (especially for $\overline{uu}$). At the center of the channel, the resolved stresses are in relatively good agreement with the DNS data, while the modeled stresses go to zero, showing that the HTLES method is well suited for reducing the contribution of the subfilter model in regions where the large-scale turbulent fluctuations are properly captured.

Finally, the study of the channel flow well supports the analytical development of the HTLES method (section 3), as well as the efficiency of the near-wall improvement to properly control the RANS-to-LES transition (section 4), showing satisfactory agreement with the reference data in regions where the LES mode is activated. In RANS mode, the behavior of the underlying RANS closure is recovered, as expected. Using the k–ω SST model herein leads to some discrepancies in the near-wall RANS region, notably regarding turbulent energy and normal stresses. To improve the results, an immediate extension of this work would be to associate the HTLES approach with an eddy-viscosity RANS model providing an accurate prediction of the turbulent energy at the wall, such as the BL–$\overline{v^2}/k$ [6]. Then, given that RANS closures based on the Boussinesq hypothesis are not suitable for accurately reproducing the flow anisotropy in the near-wall RANS region, the combination with Reynolds Stress Transport Models, such as the EB-RSM [31], would be relevant. In this perspective, additional developments are required to properly conduct the hybridization of the subfilter stress transport model.

5.3 Periodic-Hill flows

The flow over a periodical arrangement of 2D hills in a plane channel is a standard benchmark case for hybrid approaches, since the characteristics of the mean flow are governed by large-scale time-dependent phenomena, such as moving separation and reattachment points, and a recirculation region dominated by large-scale structures generated by the detached shear layer, such that RANS models are not able to satisfactorily reproduce the statistics of this flow. The flow configuration is characterized by the Reynolds number $Re_b = U_b h/\nu$, where h denotes the hill height and U_b is the bulk velocity at the hill crest. Two configurations, at $Re_b = 10600$ and 37000, are studied herein. The computational domain is $L_x \times L_y \times L_z = 9h \times 3.035h \times 4.5h$, and periodic conditions are applied in the streamwise and spanwise directions. The streamwise periodicity avoids issues linked to inlet conditions, and a constant mass flow is imposed via a source term in the momentum equation.

The periodic-hill flow at $Re_b = 10600$ is studied using 2 grids M0 and M1, which both satisfy $\Delta_y^+ \simeq 1$ at the wall. The fine grid M0 ($N_x \times N_y \times N_z = 160 \times 160 \times 80$) almost exactly corresponds to the mandatory mesh of the ATAAC project [23]. The coarse mesh M1 ($80 \times 80 \times 40$) is obtained by reducing the number of cells by a factor of two in each direction. The dimensionless grid spacing on the lower wall is described in Fig. 20. The LES with 13.1 million cells of Breuer and Jaffrézic [7] and the PIV measurements of Rapp and Manhart [38] are taken as reference solutions.

To begin with, it is interesting to emphasize the behavior of standard RANS and LES models, by studying the distribution of skin friction on the lower wall of the periodic-hill in Fig. 21. On the one hand, k–ω SST results show large differences compared to the reference data, in particular a very late reattachment. On the other hand, using the standard Smagorinsky model [43], the skin friction distribution is well predicted using the fine mesh M0, but the results are severely discrepant using M1, since this grid is too coarse compared to the LES requirements. In addition, to assess the influence of turbulence models and numerical methods separately, no-model simulations are performed. Using the fine grid M0, no-model predictions fairly well agree with the reference data, showing that a quasi-DNS calculation could be performed. In contrast, using the coarse grid M1, the no-model simulation shows several disagreements with the reference data, in the same way as for the LES calculation. These results highlight the interest of introducing a more advanced modeling of the flow when coarse grids are used.

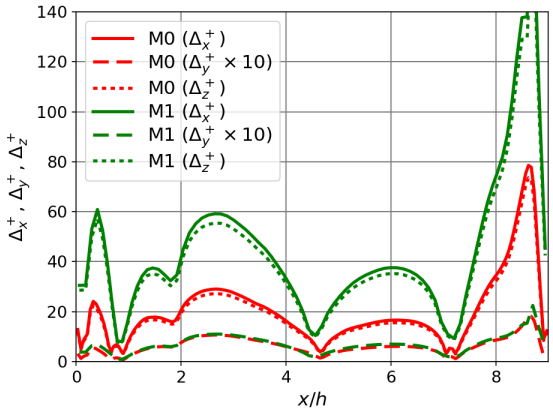

Fig. 20 Dimensionless grid spacings in wall units on the lower wall of the periodic-hill, using grids M0 and M1.

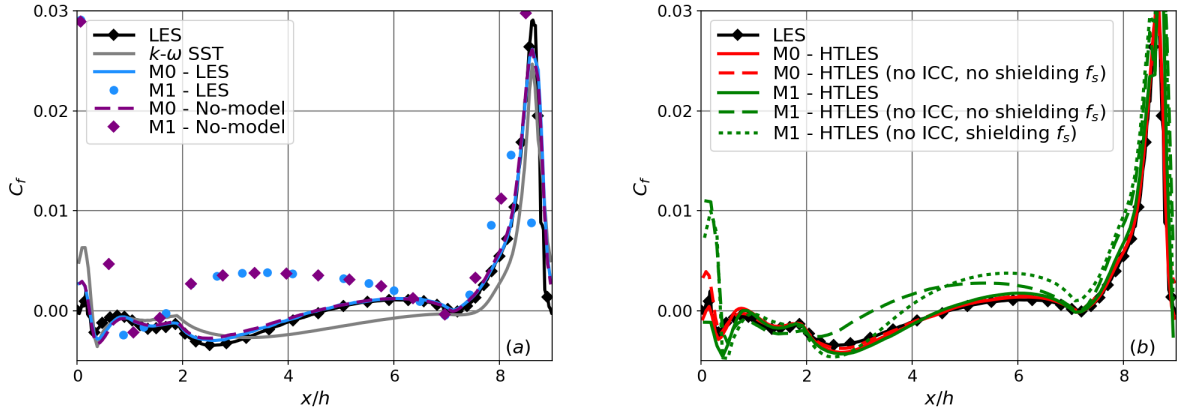

Fig. 21 Skin friction on the lower wall of the periodic-hill at $Re_b = 10600$ - k–ω SST, LES, and no-model predictions (a), and HTLES calculations (b), using grids M0 and M1.

Hence, in Fig. 21, the upgraded k–ω SST HTLES model fairly reproduces the reference data, using both fine and coarse grids. Notably, the reattachment location is predicted at $x/h \simeq 4.60$, which is close to the reference LES ($x/h \simeq 4.65$). Regarding the location of the detachment point, the use of the coarse mesh M1 leads to some discrepancies, since the tiny recirculation before the separation location is overestimated. This error underlines the importance of the grid refinement at the top of the hill ($\Delta_x/h > 0.1$ for M1), and the results are significantly improved with the fine mesh M0.

The HTLES model without shielding functions and ICC is also evaluated in Fig. 21. Using the fine grid M0, HTLES results are in reasonable agreement with reference data. Using the coarse grid M1, the RANS-to-LES switch occurs too close to the wall, and large errors are observed, which emphasizes the importance of the upgraded HTLES formulation developed in section 4. In addition, the introduction of the shielding function is necessary to enforce the RANS mode, but not sufficient to correctly recover the RANS behavior, as illustrated by the HTLES calculation with shielding but without ICC.

Attention is now focused on various profiles at different streamwise locations (extracted at $x/h = 0$, 2, 4, 6 and 8). It can be observed from Fig. 22 that, at $Re_b = 10600$, the global shielding function f_s (Eq. 39) is exactly the same for M0 and M1, since the largest extent of the shielding is due to $f_s(\xi_K)$, which is independent of the grid resolution. It is interesting to provide the exact same shielding in this case, in order to improve the robustness of HTLES regarding grid coarsening while preserving the same location of the RANS-to-LES switch. In Fig. 23, it is observed that, without shielding functions, the energy ratio defined by Eq. (21) drives the simulation towards LES very close to the wall, where the grid M1 is insufficient to apply the LES mode, which explains why the HTLES model without the shielding function and the ICC performs badly. In contrast, using the shielding functions, the transition from RANS to LES occurs far away

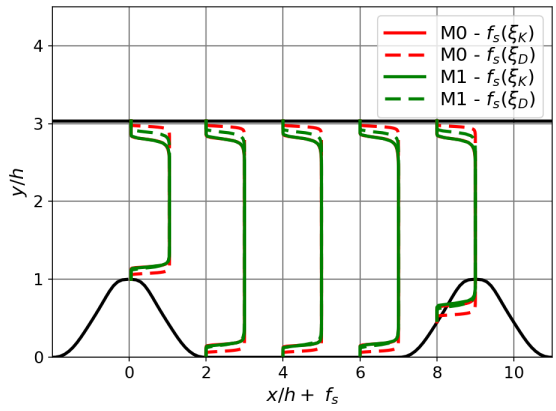

Fig. 22 Profiles of the shielding functions $f_s(\xi_K)$ and $f_s(\xi_\Delta)$, periodic-hill flow at $Re_b = 10600$.

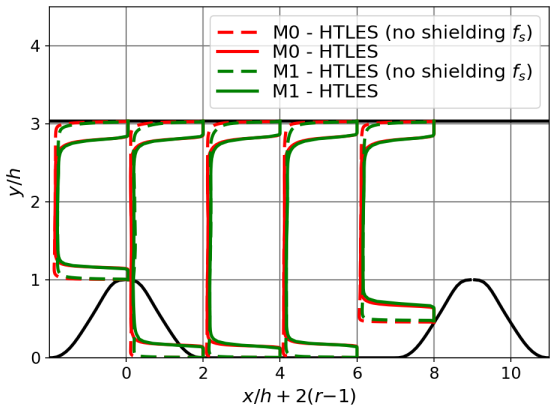

Fig. 23 Profiles of the energy ratio r with and without shielding functions, periodic-hill flow at $Re_b = 10600$.

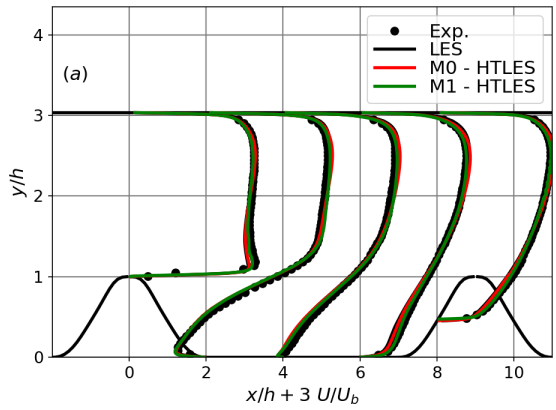

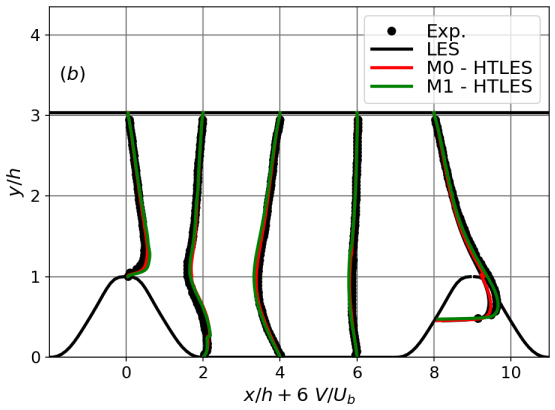

Fig. 24 Streamwise (a) and normal (b) velocity profiles, periodic-hill flow at $Re_b = 10600$. HTLES results using grids M0 and M1.

from the wall, at the same location for both grids. In the LES region, the energy ratio reaches a plateau at a value that decreases when the mesh is refined.

For the two grids, the reference data are well reproduced regarding the mean velocity and total shear stress profiles, as shown in Fig. 24 and 25-(a), respectively. Some minor differences are visible dependent on the grid resolution, but the results remain in close agreement with each other. In Fig. 25-(b,c,d), by focusing on the total Reynolds stresses, it is interesting to remark that even if a global overestimation of the turbulent energy is observed, notably in the detached shear layer, the shape of the profiles is qualitatively reproduced and the anisotropy of turbulence is captured reasonably well. Some discrepancies appear between grids M0 and M1, but the agreement is encouraging considering the large difference between the grid resolutions. Moreover, note that when the grid is refined, averaged HTLES results approach the reference averaged LES solution, as desired, although the near-wall region is still solved in RANS mode.

Finally, the streamlines obtained by averaging the velocity both in the spanwise direction and in time, are shown in Fig. 26. HTLES predictions using grids M0 and M1 are compared to the reference LES using a very fine grid. The averaged flowfield is qualitatively well reproduced, notably regarding the shape and the spatial extent of the recirculation bubble.

To evaluate the sensitivity of the model to the Reynolds number, the validation performed in the case at a higher Reynolds number $Re_b = 37000$, is shortly presented. The HTLES model is evaluated against the experimental data of Rapp and Manhart [39], using a relatively coarse mesh N1 ($160 \times 180 \times 80$). As shown by the streamlines of the averaged flowfield in Fig. 27, the shortening of the recirculation region as compared with the lower Reynolds number case is reproduced (see Fig 26). The velocity and shear stress profiles agree fairly well with the reference data in Fig. 28 and 29, respectively. In Fig. 30-(a,b), the shape of the turbulent stress profiles shows a correct trend compared with experimental results, but an overestimation of the peak in the detached shear layer is clearly visible. These HTLES predictions are similar to the results obtained with other hybrid methods associated with eddy-viscosity closures, as presented in the review of Jakirlic [23]. To improve the results, the use of a second order closure may bring some benefits,

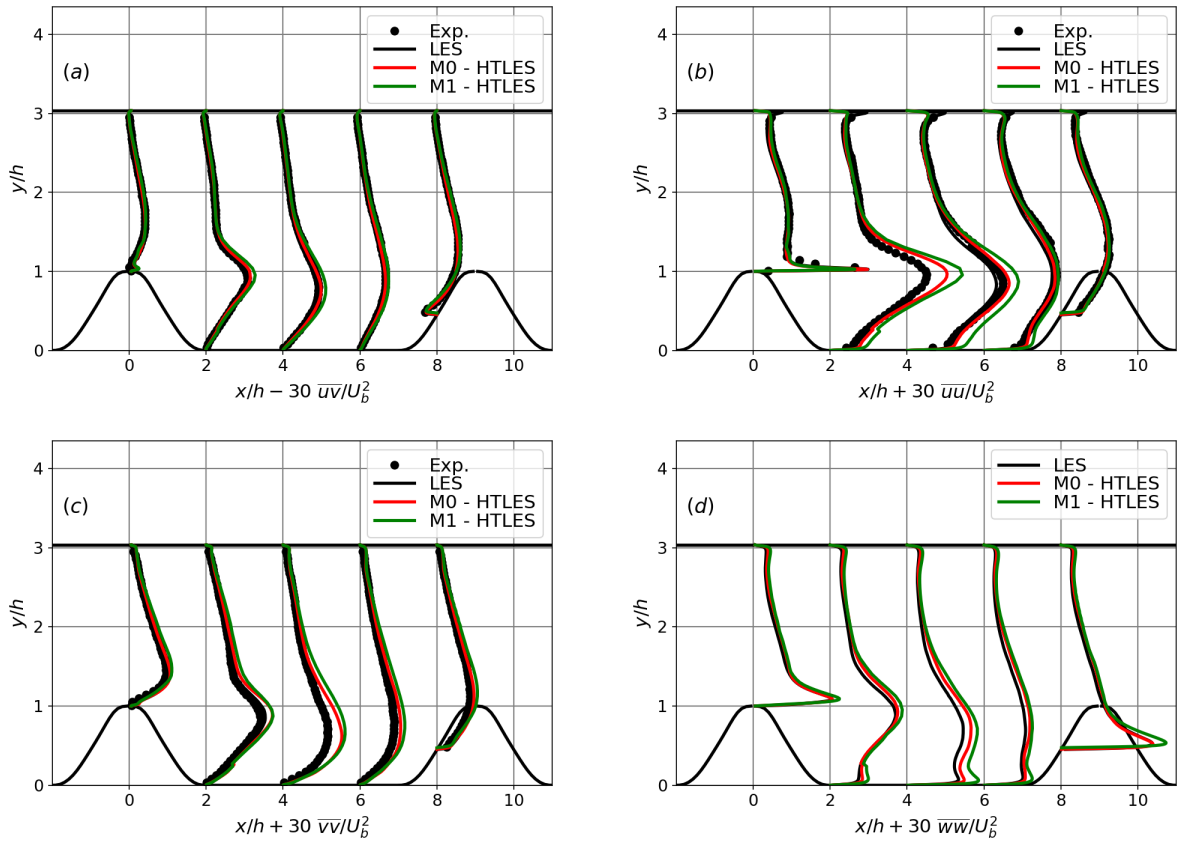

Fig. 25 Profiles of the modeled + resolved shear stess (a), streamwise (b), normal (c) and spanwise (d) components of the Reynolds stresses, periodic-hill flow at Re_b=10600. HTLES results using grids M0 and M1.

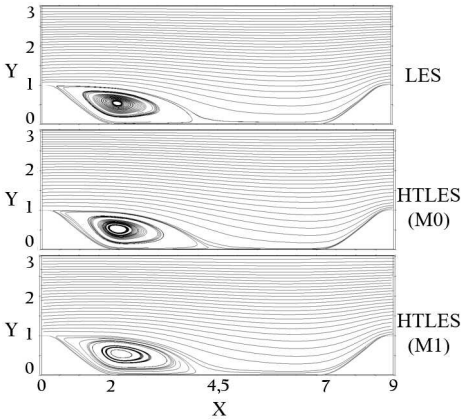

Fig. 26 Streamlines of the averaged flowfield, periodic-hill flow at Re_b=10600. Reference LES and HTLES results using grids M0 and M1.

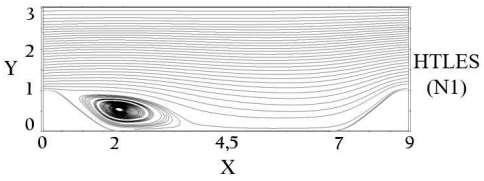

Fig. 27 Streamlines of the averaged flowfield, periodic-hill flow at Re_b=37000. HTLES results using grid N1.

notably to reproduce the turbulence anisotropy at the wall. In this regard, note that the reference PITM calculation [12] provides similar predictions regarding the velocity and shear stress profiles, but the normal turbulent stresses are fairly well recovered, suggesting that the use of a subfilter stress transport model is relevant. Nevertheless, considering that the number of cells in the x and z-direction is the same for grids M0 and N1 irrespective of the Reynolds number, the results remain in satisfactory agreement with the reference. Hence, the validation process of the HTLES model is completed, using different grid refinements and Reynolds numbers.

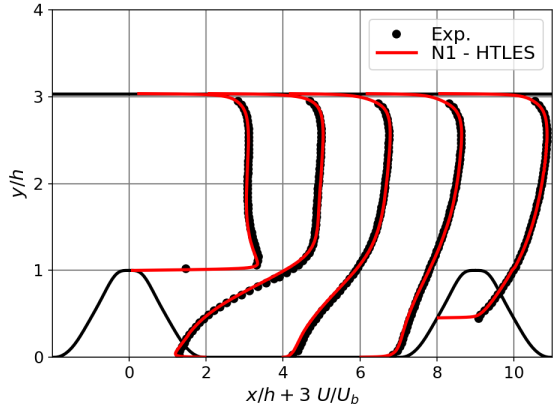

Fig. 28 Streamwise velocity profiles, periodic-hill flow at $Re_b = 37000$. HTLES results using grid N1.

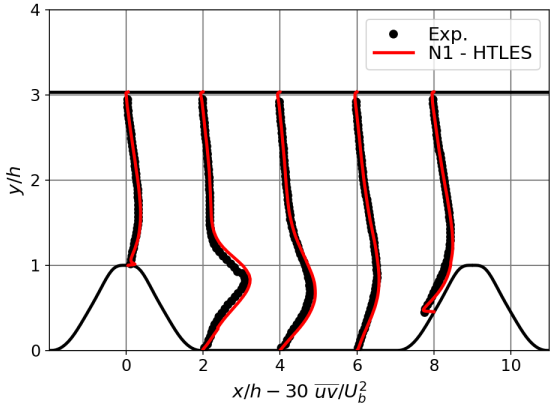

Fig. 29 Resolved + Modeled shear stress profiles $\overline{uv}$, periodic-hill flow at $Re_b = 37000$. HTLES results using grid N1.

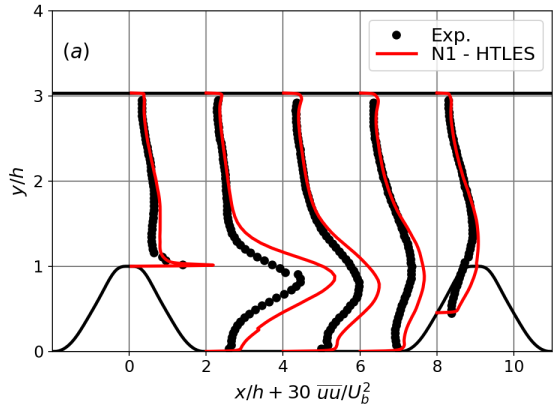

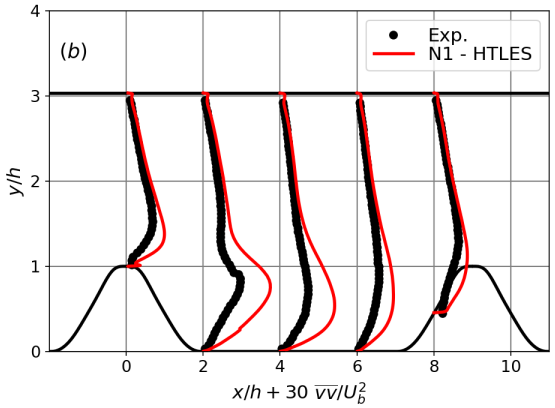

Fig. 30 Profiles of the modeled + resolved streamwise (a) and normal (b) components of the Reynolds stresses, periodic-hill flow at Re_b=37000. HTLES results using grid N1.

6 Conclusion

The present paper describes the development and validation of a continuous hybrid RANS-LES model based on temporal filtering, ensuring a consistent bridging between RANS and LES modes. The model aims at providing solid theoretical foundations and sufficient robustness for future industrial applications. Following the work of Fadai-Gothbi *et al.* [15], Friess *et al.* [16], and Manceau [30], a new formulation of the HTLES model is derived from TPITM, ensuring a Hybrid-equivalence criterion between the approaches. Notably, focusing on the destruction term of the energy equation, it is noted that the variable transported by the second equation is related the modeled dissipation rate via the hybridization function. In this context, a theoretical analysis is conducted to show that the hybridization function has to be added in the definition of the subfilter viscosity. In such a case, a more comprehensive expression of the hybridization function is obtained compared with the original formulation, showing a better consistency of the assumptions. The development of the HTLES approach is illustrated using a k–ε closure for the sake of simplicity, before extending the method to the k–ω SST model. The calibration of the model is performed in decaying isotropic turbulence, showing a good agreement of the calibrated coefficients with the values obtained from the theory.

A second part introduces several improvements of the model for wall-bounded flows. Notably, a two-fold shielding function and an internal consistency constraint are introduced.

(i) The shielding function $f_s(\xi_K)$ provides a constant protection in wall units, independent of the grid refinement or the Reynolds number. It enforces the RANS mode up to the beginning of the log layer, and prevents the model from switching to LES when the mesh is finer than a RANS mesh but not fine enough for LES.
(ii) The shielding function $f_s(\xi_D)$ depends on the maximum cell dimension, in order to adapt the location of the RANS-to-LES transition when the grid is too coarse in any of the directions compared to the distance to the wall, in order

to properly resolve the near-wall turbulent structures in LES mode, thus avoiding the appearance of a log-layer mismatch.

(iii) The internal consistency constraint is applied in order to disregard the contribution of resolved fluctuations in the turbulent energy in the RANS region, since the penetration of resolved turbulent fluctuation from the LES region into the RANS region contradicts the theoretical assumption that the resolved energy is zero in this zone.

The upgraded formulation of the model provides a suitable control of the energy partition in the boundary layer. The expected outcomes are reached, since in the near-wall region where the activation of the LES mode is not suitable, the location of the RANS-to-LES transition is appropriately set up and the RANS mode is enforced.

The predictive accuracy of the upgraded formulation of the k–ω SST HTLES model is validated in various configurations. The case of plane-channel flows is investigated over a range of Reynolds numbers, showing the correct behavior of the model in wall-bounded flows and that no log-layer mismatch is observed. These results highlight the benefit of the upgraded formulation. Since the near-wall region is solved in RANS mode, the grid resolution in the streamwise and spanwise directions are determined by the geometry, independently of the Reynolds number, which drastically decreases the numerical cost compared to LES (the cost reduction scales with Re_τ^2). The grid sensitivity study shows a significant improvement of the results for grids elongated in the streamwise direction compared to the spanwise direction. These results suggest some recommendations for designing the grid, in line with recommendations for WMLES [28]. Finally, in the near-wall region treated in RANS mode, it is worth pointing out that the behavior of the underlying RANS model is recovered, as expected.

The HTLES model succeeds in simulating the periodic-hill flow at moderate and high Reynolds numbers, providing accurate estimates of the quantities of interest, using coarse grids for which the LES results are severely discrepant with the reference data. Hence, it demonstrates the robustness of HTLES regarding grid coarsening.

HTLES appears very promising for industrial applications: benefiting from a solid and general formulation, it offers a cost-saving alternative to wall-resolved LES, providing unsteady information about the quantities of interest. Although a significant amount of empiricism is inevitably introduced in the near-wall region by the shielding functions, a theoretical link with the equations of motion is a prerequisite for the improvement of the model based on physical mechanisms. For example, the introduction of the empirical shielding function (Eq. 38) to avoid the log-layer mismatch could be avoided in the future by taking into account in an anisotropic manner in the formalism the relationship between the grid and the turbulent scales. Furthermore, in order to limit the grey area and log-layer mismatch issues, this formalism can help to identify the terms that should be introduced in the equations that are linked to the noncommutativity of the filter with the differential operators, as shown for the additive filter [18,20] and the PITM [13].

In practice, this approach bears similarities with DES, as regards the modification of the dissipation term in the turbulent energy equation, but also significant differences: in particular, it is based on a time rather than a length scale; it includes an explicit modification of the eddy-viscosity; the switch from RANS to LES is based on comparisons involving average quantities. This last aspect clearly connects the HTLES to the PITM family [10] from which it is derived. However, a major difference with the PITM is the control of the transition from RANS to LES via the k-equation rather than the ε-equation, which avoids, according to our experience, which confirms that of [14], difficulties in maintaining resolved turbulent structures in certain situations.

Future prospects concern the sensitivity of the hybrid approach to the closure, using RANS models with a particular modeling effort to reproduce wall-blockage (family of elliptic relaxation models [6,31]). Moreover, it is of interest for industrial applications to assess the capability of HTLES to resolve wall-pressure fluctuations.

7 Appendix

7.1 Perturbation analysis to ensure H-equivalence between TPITM and HTLES

Postulating that *Two hybrid approaches based on the same closure, but using different method of control of the energy partition, yield similar low-order statistics of the resolved velocity fields provided that they yield the same level of subfilter energy* [16], the H-equivalence between the TPITM system Eq. (9, 10) and the HTLES system Eq. (12, 18) is ensured if the two methods tend to the same closure when the filter width is going to infinity and lead to the same energy partition for a particular situation. Hence, using a k–ε closure herein, the objective of the analysis is to identify the relation between the hybridization functions $C_{\varepsilon 2}^P(r)$ and $\psi(r)$, to provide the same level of modeled energy k_m.

Departing from the RANS limit where the H-equivalence is ensured ($k_\mathrm{m} = k$), infinitesimal perturbations of the hybridization functions $\delta C_{\varepsilon 2}^P$ and $\delta\psi$ are introduced into the TPITM and HTLES systems, which remain H-Equivalent as long as the same infinitesimal variation δk_m of the modeled energy is obtained. The perturbation analysis can be carried out in some particular situations, following Friess *et al.* [16]. Calculations are conducted herein in the less restrictive situation: inhomogeneous turbulence in straight duct flows. In this case, both modeled energy and dissipation

are in equilibrium along streamlines, which leads to the following system of equations for HTLES,

$$\nu_{\mathrm{m}} = C_\mu \frac{k_{\mathrm{m}}^2}{\psi(r)\varepsilon_{\mathrm{m}}^*}, \qquad \begin{cases} 0 = P_{\mathrm{m}} + D_{k\mathrm{m}} - \psi(r)\varepsilon_{\mathrm{m}}^*, \\ 0 = C_{\varepsilon 1}\dfrac{\varepsilon_{\mathrm{m}}^*}{k_{\mathrm{m}}}P_{\mathrm{m}} + D_{\varepsilon\mathrm{m}}^* - C_{\varepsilon 2}\dfrac{\varepsilon_{\mathrm{m}}^{*\,2}}{k_{\mathrm{m}}}. \end{cases} \tag{41}$$

Introducing an infinitesimal perturbation $\delta\psi$ of the coefficient $\psi(r)$ in the equation results in infinitesimal variations of the solution, such that the following relation is obtained,

$$\begin{cases} 0 = \delta P_{\mathrm{m}} + \delta D_{k\mathrm{m}} - \left(\dfrac{\delta\psi}{\psi(r)} + \dfrac{\delta\varepsilon_{\mathrm{m}}^*}{\varepsilon_{\mathrm{m}}^*}\right)\psi(r)\varepsilon_{\mathrm{m}}^*, \\ 0 = C_{\varepsilon 1}\dfrac{\varepsilon_{\mathrm{m}}^*}{k_{\mathrm{m}}}P_{\mathrm{m}}\left(\dfrac{\delta P_{\mathrm{m}}}{P_{\mathrm{m}}} + \dfrac{\delta\varepsilon_{\mathrm{m}}^*}{\varepsilon_{\mathrm{m}}^*} - \dfrac{\delta k_{\mathrm{m}}}{k_{\mathrm{m}}}\right) + \delta D_{\varepsilon\mathrm{m}}^* - C_{\varepsilon 2}\dfrac{\varepsilon_{\mathrm{m}}^{*\,2}}{k_{\mathrm{m}}}\left(2\dfrac{\delta\varepsilon_{\mathrm{m}}^*}{\varepsilon_{\mathrm{m}}^*} - \dfrac{\delta k_{\mathrm{m}}}{k_{\mathrm{m}}}\right). \end{cases} \tag{42}$$

The diffusion terms are given by the gradient-diffusion hypothesis with the usual coefficients σ_k and σ_ε,

$$\begin{cases} D_{k\mathrm{m}} = \dfrac{\partial}{\partial x_k}\left(\dfrac{C_\mu}{\sigma_k}\dfrac{k_{\mathrm{m}}^2}{\psi(r)\varepsilon_{\mathrm{m}}^*}\dfrac{\partial k_{\mathrm{m}}}{\partial x_k}\right), \\ D_{\varepsilon\mathrm{m}}^* = \dfrac{\partial}{\partial x_k}\left(\dfrac{C_\mu}{\sigma_\varepsilon}\dfrac{k_{\mathrm{m}}^2}{\psi(r)\varepsilon_{\mathrm{m}}^*}\dfrac{\partial \varepsilon_{\mathrm{m}}^*}{\partial x_k}\right), \end{cases} \quad \text{such that} \quad \begin{cases} \dfrac{\delta D_{k\mathrm{m}}}{D_{k\mathrm{m}}} = 3\dfrac{\delta k_{\mathrm{m}}}{k_{\mathrm{m}}} - \dfrac{\delta\varepsilon_{\mathrm{m}}^*}{\varepsilon_{\mathrm{m}}^*} - \dfrac{\delta\psi}{\psi(r)}, \\ \dfrac{\delta D_{\varepsilon\mathrm{m}}^*}{D_{\varepsilon\mathrm{m}}^*} = 2\dfrac{\delta k_{\mathrm{m}}}{k_{\mathrm{m}}} - \dfrac{\delta\psi}{\psi(r)}. \end{cases} \tag{43}$$

Moreover, in eddy-viscosity models the production term is given by,

$$P_{\mathrm{m}} = 2\gamma C_\mu \frac{k_{\mathrm{m}}^2}{\psi(r)\varepsilon_{\mathrm{m}}^*}S^2, \tag{44}$$

where S is the statistical averaged of the rate of strain, and $\gamma = \overline{P_{\mathrm{sfs}}}/P_{\mathrm{m}}$ is a correlation coefficient. Then, the perturbation analysis is applied, leading to

$$\frac{\delta P_{\mathrm{m}}}{P_{\mathrm{m}}} = \frac{\delta\gamma}{\gamma} + 2\frac{\delta S}{S} + 2\frac{\delta k_{\mathrm{m}}}{k_{\mathrm{m}}} - \frac{\delta\varepsilon_{\mathrm{m}}^*}{\varepsilon_{\mathrm{m}}^*} - \frac{\delta\psi}{\psi(r)}. \tag{45}$$

Finally, the previous equations (43, 45) are introduced into the system of equations (42), which yields

$$\delta\psi = -\frac{(C_{\varepsilon 2} - C_{\varepsilon 1}\psi(r))\,\psi(r)}{C_{\varepsilon 2}}\frac{P_{\mathrm{m}}}{\psi(r)\varepsilon_{\mathrm{m}}^*}\left(\frac{\delta k_{\mathrm{m}}}{k_{\mathrm{m}}} - \frac{\delta\gamma}{\gamma} - 2\frac{\delta S}{S}\right). \tag{46}$$

A similar analysis can be conducted for TPITM (see [16] for details), and the following relation is obtained

$$\delta C_{\varepsilon 2}^P = (C_{\varepsilon 2}^P(r) - C_{\varepsilon 1})\frac{P_{\mathrm{m}}}{\varepsilon_{\mathrm{m}}}\left(\frac{\delta k_{\mathrm{m}}}{k_{\mathrm{m}}} - \frac{\delta\gamma}{\gamma} - 2\frac{\delta S}{S}\right). \tag{47}$$

Applying the H-equivalence postulate [16], i.e. the same modification δk_{m} of the modeled energy leads to the same infinitesimal variation of the low-order statistics (δS, $\delta\gamma$), and recalling the equality $\varepsilon_{\mathrm{m}} = \psi(r)\varepsilon_{\mathrm{m}}^*$ (Eq. 17), then if HTLES and TPITM are H-Equivalent for some initial values of $\psi(r)$ and $C_{\varepsilon 2}^P(r)$, they remain equivalent if the infinitesimal perturbations of their hybridization functions expressed by Eq. (46) and (47) satisfy the relation

$$\frac{\delta C_{\varepsilon 2}^P}{\left(C_{\varepsilon 2}^P(r) - C_{\varepsilon 1}\right)} = -\frac{C_{\varepsilon 2}\delta\psi}{(C_{\varepsilon 2} - C_{\varepsilon 1}\psi(r))\,\psi(r)}. \tag{48}$$

Lastly, the previous formula is integrated between the RANS state ($r = 1$, $C_{\varepsilon 2}^*(1) = C_{\varepsilon 2}$, $\psi(1) = 1$) and some arbitrary LES state, such that

$$\int_{C_{\varepsilon 2}}^{C_{\varepsilon 2}^P}\frac{1}{x - C_{\varepsilon 1}}\mathrm{d}x = -\int_1^{\psi}\frac{C_{\varepsilon 2}}{(C_{\varepsilon 2} - C_{\varepsilon 1}y)y}\mathrm{d}y, \tag{49}$$

and simple algebra leads to

$$\psi(r) = \frac{C_{\varepsilon 2}}{C_{\varepsilon 2}^P(r)} = \frac{C_{\varepsilon 2}}{C_{\varepsilon 1} + r(C_{\varepsilon 2} - C_{\varepsilon 1})}. \tag{50}$$

In the other situations considered in Friess *et al.* [16], it is assumed that the modeled dissipation rate is not affected by the modification of the energy partition, such that $\delta\varepsilon_{\mathrm{m}} = \delta(\psi(r)\varepsilon_{\mathrm{m}}^*) = 0$ (Eq. 17). Calculations are much simpler in this way and the same formulation of $\psi(r)$ is obtained (not shown here) .

7.2 H-equivalence between TPITM and HTLES based on SST closure

In this section, the k–ω SST HTLES formulation is derived from k–ω SST TPITM, while preserving the H-equivalence criterion. In the k–ω SST TPITM model, developed by Bentaleb *et al.* [5], the modeled viscosity ν_m, energy k_m and specific dissipation ω_m, satisfy

$$\nu_\mathrm{m} = \frac{k_\mathrm{m}}{\omega_\mathrm{m}}, \qquad \begin{cases} \dfrac{Dk_\mathrm{m}}{Dt} &= P_\mathrm{m} + D_{k\mathrm{m}} - C_\mu k_\mathrm{m}\omega_\mathrm{m}, \\ \dfrac{D\omega_\mathrm{m}}{Dt} &= \gamma_\omega \dfrac{\omega_\mathrm{m}}{k_\mathrm{m}} P_\mathrm{m} + D_{\omega\mathrm{m}} - \beta_\omega^P {\omega_\mathrm{m}}^2 + C_{\omega\mathrm{m}}, \end{cases} \tag{51}$$

where $D_{\omega\mathrm{m}}$ stand for the diffusion of ω_m, $C_{\omega\mathrm{m}}$ is the cross-diffusion term, $\gamma_\omega = C_{\varepsilon 1} - 1$ and $\beta_\omega = C_\mu(C_{\varepsilon 2} - 1)$ are the usual coefficients, and the hybridization term β_ω^P is defined by

$$\beta_\omega^P(r) = C_\mu \gamma_\omega + r(\beta_\omega - C_\mu \gamma_\omega). \tag{52}$$

The k–ω SST HTLES model is derived by transferring the new hybridization function $\psi'(r)$ in the modeled energy equation and introducing a new variable ω_m^* transported by the second equation, in the same way as for the derivation of the k–ε HTLES in section 3.1, such that

$$\nu_\mathrm{m} = \frac{k_\mathrm{m}}{\psi'(r)\omega_\mathrm{m}^*}, \qquad \begin{cases} \dfrac{Dk_\mathrm{m}}{Dt} &= P_\mathrm{m} + D_{k\mathrm{m}} - C_\mu k_\mathrm{m}\psi'(r)\omega_\mathrm{m}^*, \\ \dfrac{D\omega_\mathrm{m}^*}{Dt} &= \gamma_\omega \dfrac{\omega_\mathrm{m}^*}{k_\mathrm{m}} P_\mathrm{m} + D_{\omega\mathrm{m}}^* - \beta_\omega {\omega_\mathrm{m}^*}^2 + C_{\omega\mathrm{m}}^*, \end{cases} \tag{53}$$

where $D_{\omega\mathrm{m}}^*$ stands for the diffusion of ω_m^*.

Similar to the case of the k–ε model, the perturbation analysis is carried out to ensure H-equivalence. The calculations (not shown here) are very similar to those presented in Appendix 7.1, leading to the new expression of the hybridization function

$$\psi'(r) = \frac{\beta_\omega}{\beta_\omega^P(r)} = \frac{\beta_\omega}{C_\mu\gamma_\omega + r(\beta_\omega - C_\mu\gamma_\omega)}. \tag{54}$$

Again, it is noted that the same formulation of $\psi'(r)$ is obtained, irrespective of the situations proposed by Friess *et al.* [16] to conduct the perturbation analysis (not shown here).

7.3 The k–ω SST HTLES model

The k–ω SST HTLES formulation is given by :

$$\nu_\mathrm{sfs} = \frac{a_1 k_\mathrm{sfs}}{\max\left[a_1\psi'(r)\omega_\mathrm{sfs}^*, F_2\widetilde{S}\right]}, \tag{55}$$

$$\begin{cases} \dfrac{\partial k_\mathrm{sfs}}{\partial t} + \widetilde{U}_j\dfrac{\partial k_\mathrm{sfs}}{\partial x_j} &= P_k + \dfrac{\partial}{\partial x_j}\left[\left(\nu + \dfrac{\nu_\mathrm{sfs}}{\sigma_k}\right)\dfrac{\partial k_\mathrm{sfs}}{\partial x_j}\right] - \dfrac{k_\mathrm{sfs}}{T_\mathrm{m}}, \\ \dfrac{\partial \omega_\mathrm{sfs}^*}{\partial t} + \widetilde{U}_j\dfrac{\partial \omega_\mathrm{sfs}^*}{\partial x_j} &= \gamma_\omega\dfrac{1}{\psi'(r)}\widetilde{S}^2 + \dfrac{\partial}{\partial x_j}\left[\left(\nu + \dfrac{\nu_\mathrm{sfs}}{\sigma_\omega}\right)\dfrac{\partial \omega_\mathrm{sfs}^*}{\partial x_j}\right] - \beta_\omega {\omega_\mathrm{sfs}^*}^2 \\ & \quad + (1-F_1)2\dfrac{1}{\sigma_{\omega 2}}\dfrac{1}{\psi'(r)\omega_\mathrm{sfs}^*}\dfrac{\partial \omega_\mathrm{sfs}^*}{\partial x_j}\dfrac{\partial k_\mathrm{sfs}}{\partial x_j}, \end{cases} \tag{56}$$

where the production limiter is defined as :

$$P_k = \min\left[\nu_\mathrm{sfs}\widetilde{S}^2, a_2 C_\mu k_\mathrm{sfs}\psi'(r)\omega_\mathrm{sfs}^*\right], \tag{57}$$

and the function F_1 and F_2 are the blending functions (not modified in the hybrid context), and γ_ω, β_ω, a_1, a_2, σ_k, σ_ω are the usual coefficients dependent of the branch of the k–ω SST model.

The hybridization of the model is carried out by the energy ratio r, via the function $\psi'(r)$ and the time scale T_m, applying the shielding functions and the internal consistency constraint, such that

$$T_\mathrm{m} = \frac{r}{\psi'(r)}\frac{k_\mathrm{m} + c_r k_\mathrm{r}}{C_\mu k_\mathrm{m}\omega_\mathrm{m}^*}, \qquad \text{where } c_r = \begin{cases} 0 \text{ if } r = 1, \\ f_s \text{ if } r < 1, \end{cases} \tag{58}$$

$$\psi'(r) = \frac{\beta_\omega}{C_\mu \gamma_\omega + r(\beta_\omega - C_\mu \gamma_\omega)}, \tag{59}$$

$$r = (1 - f_s) \times 1 + f_s \times \min[1, r_K], \tag{60}$$

$$r_K = \frac{1}{\beta_0}\left(\frac{U_s}{\sqrt{k}}\right)^{2/3}\left(\omega_c \frac{k}{\varepsilon}\right)^{-2/3} \quad \text{where } \omega_c = \min\left[\frac{\pi}{dt}, \frac{U_s \pi}{\Delta}\right],\ U_s = U + \gamma\sqrt{k} \text{ and } \Delta = \Omega^{1/3}, \tag{61}$$

where Ω is the volume of the cell,

$$f_s = 1 - \tanh\left[\max\left[\xi_K^{p_1}, \xi_D^{p_2}\right]\right], \tag{62}$$

$$\xi_K = C_1 \frac{(\nu^3/\varepsilon)^{1/4}}{d_w} \quad \text{and} \quad \xi_D = C_2 \frac{\Delta_{\max}}{d_w}, \quad \text{where } \Delta_{\max} = \max\left[\Delta_x, \Delta_y, \Delta_z\right], \tag{63}$$

and the statistically-averaged energy and dissipation terms are estimated as

$$k = k_{\mathrm{m}} + k_{\mathrm{r}} \quad \text{and} \quad \varepsilon = \varepsilon_{\mathrm{m}} = C_\mu k_{\mathrm{m}} \psi'(r) \omega_{\mathrm{m}}^*. \tag{64}$$

The estimates of statistically-averaged quantities $\overline{f}$ are provided by an exponentially-weighted average [37], with a time filter width Δ_T corresponding to several tens of flow-through times herein, such that

$$\frac{\partial \overline{f}(t, \Delta_T)}{\partial t} = \frac{\widetilde{f}(t) - \overline{f}(t, \Delta_T)}{\Delta_T}. \tag{65}$$

Table 3 Coefficients of the k–ω SST HTLES model.

β_0	γ	C_1	C_2	p_1	p_2
0.48	2/3	45	1.2	8	6

Acknowledgements This work was partially supported by the ANRT (CIFRE contract 2017/0963) and the ANR project MONACO_2025 (ANR-17-CE06-0005-01_ACT). This article is dedicated to our dear colleague and friend Tom Gatski.

Compliance with ethical standards

Funding This study was funded by the ANRT (CIFRE contract 2017/0963) and the ANR project MONACO_2025 (reference number ANR-17-CE06-0005-01_ACT).

Conflit of Interest The authors declare that they have no conflict of interest.

References

1. Afailal, A.H.: Numerical simulation of non-reactive aerodynamics in internal combustion engines using a hybrid RANS/LES approach. Ph.D. thesis, Université de Pau et des pays de l'Adour (2020)
2. Afailal, H., Galpin, J., Velghe, A., Manceau, R.: Development and validation of a hybrid temporal LES model in the perspective of applications to internal combustion engines. Oil Gas Sci. Technol. **74** (2019)
3. Archambeau, F., Méchitoua, N., Sakiz, M.: Code Saturne: A finite volume code for the computation of turbulent incompressible flows-Industrial applications. International Journal on Finite Volumes (2004)
4. Ashton, N., Prosser, R., Revell, A.: A hybrid numerical scheme for a new formulation of delayed detached-eddy simulation (DDES) based on elliptic relaxation. In: Journal of Physics: Conference Series, vol. 318, p. 042043. IOP Publishing (2011)
5. Bentaleb, Y., Manceau, R.: A hybrid temporal LES/RANS formulation based on a two-equation subfilter model. In: TSFP Digital Library Online. Begel House Inc. (2011)
6. Billard, F., Laurence, D.: A robust k-ε-$\overline{v^2}/k$ elliptic blending turbulence model applied to near-wall, separated and buoyant flows. International Journal of Heat and Fluid Flow **33**(1), 45–58 (2012)
7. Breuer, M., Jaffrézic, B.: New reference data for the hill flow test case. ERCOFTAC QNET-CFD Knowledge Base Wiki: http://www.ercoftac.org/products_and_services/wiki (2005)
8. Chaouat, B.: Subfilter-scale transport model for hybrid RANS/LES simulations applied to a complex bounded flow. Journal of Turbulence (11), N51 (2010)

9. Chaouat, B.: The state of the art of hybrid RANS/LES modeling for the simulation of turbulent flows. Flow, turbulence and combustion **99**(2), 279–327 (2017)
10. Chaouat, B., Schiestel, R.: A new partially integrated transport model for subgrid-scale stresses and dissipation rate for turbulent developing flows. Physics of Fluids **17**(6), 065106 (2005)
11. Chaouat, B., Schiestel, R.: Progress in subgrid-scale transport modelling for continuous hybrid non-zonal RANS/LES simulations. Int. J. Heat Fluid Fl. **30**(4), 602–616 (2009)
12. Chaouat, B., Schiestel, R.: Hybrid RANS/LES simulations of the turbulent flow over periodic hills at high Reynolds number using the PITM method. Computers & Fluids **84**, 279–300 (2013)
13. Chaouat, B., Schiestel, R.: Partially integrated transport modeling method for turbulence simulation with variable filters. Phys. Fluids **25** (2013)
14. Fadai-Ghotbi, A., Friess, C., Manceau, R., Borée, J.: A seamless hybrid RANS-LES model based on transport equations for the subgrid stresses and elliptic blending. Physics of Fluids **22**(5), 055104 (2010)
15. Fadai-Ghotbi, A., Friess, C., Manceau, R., Gatski, T.B., Borée, J.: Temporal filtering: A consistent formalism for seamless hybrid RANS–LES modeling in inhomogeneous turbulence. International Journal of Heat and Fluid Flow **31**(3), 378–389 (2010)
16. Friess, C., Manceau, R., Gatski, T.: Toward an equivalence criterion for hybrid RANS/LES methods. Computers & Fluids **122**, 233–246 (2015)
17. Germano, M.: Turbulence: the filtering approach. Journal of Fluid Mechanics **238**, 325–336 (1992)
18. Germano, M.: Properties of the hybrid RANS/LES filter. Theor. Comput. Fluid Dyn. **17**, 225–231 (2004)
19. Girimaji, S.S.: Partially-Averaged Navier-Stokes model for turbulence: A Reynolds-Averaged Navier-Stokes to Direct Numerical Simulation bridging method. Journal of Applied Mechanics **73**, 413 (2006)
20. Hamba, F.: Log-layer mismatch and commutation error in hybrid RANS/LES simulation of channel flow. Int. J. Heat Fluid Fl. **30**(1), 20–31 (2009)
21. Han, Y., He, Y., Le, J.: Modification to improved delayed detached-eddy simulation regarding the log-layer mismatch. AIAA Journal **58**(2), 712–721 (2020)
22. Hinze, J.: Turbulence, 2^{nd} edition. MacGraw Hill, New-York (1975)
23. Jakirlic, S.: Assessment of the RSM, URANS and hybrid models with respect to the different roadmaps including the industrial application challenges. Deliverable **3**, 2–36 (2012)
24. Jamal, T., Walters, D.K.: A dynamic time filtering technique for hybrid RANS-LES simulation of non-stationary turbulent flow. In: Fluids Engineering Division Summer Meeting, vol. 59032, p. V002T02A051. American Society of Mechanical Engineers (2019)
25. Jones, W., Launder, B.E.: The prediction of laminarization with a two-equation model of turbulence. International journal of heat and mass transfer **15**(2), 301–314 (1972)
26. Kang, H.S., Chester, S., Meneveau, C.: Decaying turbulence in an active-grid-generated flow and comparisons with large-eddy simulation. Journal of Fluid Mechanics **480**, 129–160 (2003)
27. Keating, A., Piomelli, U.: A dynamic stochastic forcing method as a wall-layer model for large-eddy simulation. Journal of Turbulence (7), N12 (2006)
28. Larsson, J., Kawai, S., Bodart, J., Bermejo-Moreno, I.: Large eddy simulation with modeled wall-stress: recent progress and future directions. Mechanical Engineering Reviews **3**(1), 15–00418 (2016)
29. Lee, M., Moser, R.D.: Direct numerical simulation of turbulent channel flow up to $Re_\tau \approx 5200$. Journal of Fluid Mechanics **774**, 395–415 (2015)
30. Manceau, R.: Progress in Hybrid Temporal LES. In: the 6th Symp. Hybrid RANS-LES Methods, 26–28 September 2016, Strasbourg, France, *Notes on Numerical Fluid Mechanics and Multidisciplinary Design*, vol. 137, pp. 9–25. Springer (2018)
31. Manceau, R., Hanjalić, K.: Elliptic blending model: A new near-wall Reynolds-stress turbulence closure. Physics of Fluids **14**(2), 744–754 (2002)
32. Menter, F., Egorov, Y.: A scale adaptive simulation model using two-equation models. In: 43rd AIAA aerospace sciences meeting and exhibit, p. 1095 (2005)
33. Menter, F.R.: Two-equation eddy-viscosity turbulence models for engineering applications. AIAA journal **32**(8), 1598–1605 (1994)
34. Moser, R.D., Kim, J., Mansour, N.N.: Direct numerical simulation of turbulent channel flow up to Re_τ= 590. Physics of fluids **11**(4), 943–945 (1999)
35. Nikitin, N., Nicoud, F., Wasistho, B., Squires, K., Spalart, P.R.: An approach to wall modeling in large-eddy simulations. Physics of fluids **12**(7), 1629–1632 (2000)
36. Pope, S.B.: Turbulent flows. Cambridge University Press (2001)
37. Pruett, C., Gatski, T., Grosch, C.E., Thacker, W.: The temporally filtered Navier–Stokes equations: properties of the residual stress. Physics of Fluids **15**(8), 2127–2140 (2003)
38. Rapp, C., Manhart, M.: Experimental investigations on the turbulent flow over a periodic hill geometry. In: TSFP Digital Library Online. Begel House Inc. (2007)
39. Rapp, C., Manhart, M.: Flow over periodic hills: an experimental study. Experiments in fluids **51**(1), 247–269 (2011)
40. Sagaut, P.: Large eddy simulation for incompressible flows, third edn. Springer (2006)
41. Schiestel, R., Dejoan, A.: Towards a new partially integrated transport model for coarse grid and unsteady turbulent flow simulations. Theoretical and Computational Fluid Dynamics **18**(6), 443–468 (2005)
42. Shur, M.L., Spalart, P.R., Strelets, M.K., Travin, A.K.: A hybrid RANS-LES approach with delayed-DES and wall-modelled LES capabilities. International Journal of Heat and Fluid Flow **29**(6), 1638–1649 (2008)
43. Smagorinsky, J.: General circulation experiments with the primitive equations: I. the basic experiment. Monthly weather review **91**(3), 99–164 (1963)
44. Spalart, P.: Detached-eddy simulation. Annu. Rev. Fluid Mech. **41**, 181–202 (2009)
45. Spalart, P., Jou, W., Strelets, M., Allmaras, S.: Comments on the feasibility of LES for wings, and on a hybrid RANS/LES approach. 1st AFOSR int. In: Symp. Eng. Turb. Modelling and Measurements, May, pp. 24–26 (1997)
46. Spalart, P.R.: Strategies for turbulence modelling and simulations. International Journal of Heat and Fluid Flow **21**(3), 252–263 (2000)
47. Spalart, P.R., Deck, S., Shur, M.L., Squires, K.D., Strelets, M.K., Travin, A.: A new version of detached-eddy simulation, resistant to ambiguous grid densities. Theoretical and computational fluid dynamics **20**(3), 181 (2006)
48. Tennekes, H.: Eulerian and Lagrangian time microscales in isotropic turbulence. Journal of Fluid Mechanics **67**(3), 561–567 (1975)
49. Tran, T., Manceau, R., Perrin, R., Borée, J., Nguyen, A.: A hybrid temporal LES approach. Application to flows around rectangular cylinders. In: Proceedings of 9th ERCOFTAC International Symposium on Engineering Turbulence Modelling and Measurements, Thessaloniki, Greece (2012)
50. Travin, A., Shur, M., Strelets, M., Spalart, P.: Physical and numerical upgrades in the detached-eddy simulation of complex turbulent flows. In: Advances in LES of complex flows, pp. 239–254. Springer (2002)